

CERN-EP-2018-060
2018/12/20

CMS-HIG-16-040

Measurements of Higgs boson properties in the diphoton decay channel in proton-proton collisions at $\sqrt{s} = 13$ TeV

The CMS Collaboration*

Abstract

Measurements of Higgs boson properties in the $H \rightarrow \gamma\gamma$ decay channel are reported. The analysis is based on data collected by the CMS experiment in proton-proton collisions at $\sqrt{s} = 13$ TeV during the 2016 LHC running period, corresponding to an integrated luminosity of 35.9 fb^{-1} . Allowing the Higgs mass to float, the measurement yields a signal strength relative to the standard model prediction of $1.18_{-0.14}^{+0.17} = 1.18_{-0.11}^{+0.12} (\text{stat})_{-0.07}^{+0.09} (\text{syst})_{-0.06}^{+0.07} (\text{theo})$, which is largely insensitive to the exact Higgs mass around 125 GeV. Signal strengths associated with the different Higgs boson production mechanisms, couplings to bosons and fermions, and effective couplings to photons and gluons are also measured.

Published in the Journal of High Energy Physics as doi:10.1007/JHEP11(2018)185.

arXiv:1804.02716v2 [hep-ex] 19 Dec 2018

1 Introduction

The standard model of particle physics (SM) [1–3] has been very successful in explaining the interactions between elementary particles. During the Run 1 period (2010–2012) of the CERN LHC, with proton-proton collisions at centre-of-mass energies of 7 and 8 TeV, a new particle was discovered by the ATLAS [4] and CMS [5, 6] Collaborations. The discovery was followed by a comprehensive set of studies of the properties of this new boson in the decay channels and production modes accessible with the LHC Run 1 data set. Measurements from ATLAS and CMS [7, 8] have shown that the properties of the new boson are consistent with expectations for the SM Higgs boson [9–14].

Despite the small branching fraction predicted by the SM ($\approx 0.2\%$), the $H \rightarrow \gamma\gamma$ decay channel provides a clean final state with an invariant mass peak that can be reconstructed with high precision. As a consequence, $H \rightarrow \gamma\gamma$ was one of the most important channels for the discovery of the Higgs boson and first measurements of its properties [15, 16]. In Run 2, with proton-proton collisions at $\sqrt{s} = 13$ TeV, this channel remains one of the most sensitive to continue the precise characterization of the Higgs boson.

In this paper, measurements of the Higgs boson production rates with respect to the SM prediction (signal strength modifiers) are presented, along with measurements of the coupling modifiers to fermions and bosons, and effective coupling modifiers to photons and gluons, in the so-called κ framework [17]. Improved precision on these parameters constrains possible deviations in the Higgs sector of the SM. The analysis is based on proton-proton collision data collected at $\sqrt{s} = 13$ TeV by the CMS experiment in 2016, corresponding to an integrated luminosity of 35.9 fb^{-1} .

2 The CMS detector

The central feature of the CMS apparatus is a superconducting solenoid, 13 m in length and with an inner diameter of 6 m, which provides an axial magnetic field of 3.8 T. Within the solenoid volume are a silicon pixel and strip tracker, a lead tungstate crystal electromagnetic calorimeter (ECAL), and a brass and scintillator hadron calorimeter (HCAL), each composed of a barrel and two endcap sections. Forward calorimeters extend the pseudorapidity (η) coverage provided by the barrel and endcap detectors. Muons are detected in gas-ionization chambers embedded in the steel flux-return yoke outside the solenoid.

Charged-particle trajectories are measured by the silicon pixel and strip tracker, with full azimuthal coverage within $|\eta| < 2.5$. The ECAL and HCAL surround the tracking volume and cover the region $|\eta| < 3.0$. The ECAL barrel extends to $|\eta| < 1.48$, while the endcaps cover the region $1.48 < |\eta| < 3.0$. A lead/silicon-strip preshower detector is located in front of the ECAL endcap in the region $1.65 < |\eta| < 2.6$. The preshower detector includes two planes of silicon sensors measuring the x and y coordinates of the impinging particles. A steel/quartz-fibre Cherenkov forward calorimeter extends the calorimetric coverage to $|\eta| < 5.0$. In the region $|\eta| < 1.74$, the HCAL cells have widths of 0.087 in both pseudorapidity and azimuth (ϕ). In the (η, ϕ) plane, and for $|\eta| < 1.48$, the HCAL cells map on to 5×5 ECAL crystal arrays to form calorimeter towers projecting radially outwards from points slightly offset from the nominal interaction point. In the endcap, the ECAL arrays matching the HCAL cells contain fewer crystals. The calibration of the ECAL uses the azimuthal symmetry of the energy flow in minimum-bias events, $\pi^0 \rightarrow \gamma\gamma$, $\eta \rightarrow \gamma\gamma$, $W \rightarrow e\nu$, and $Z \rightarrow e^+e^-$ decays. Changes in the response of the ECAL crystals due to irradiation during the LHC running periods and their subsequent recovery are monitored continuously and corrected for, using light injected from a

laser system. More details on the methods employed are given in Ref. [18].

The global event reconstruction algorithm, also called particle-flow event reconstruction [19], attempts to reconstruct and identify individual particles using an optimized combination of information from the various elements of the CMS detector. The energy of photons is directly obtained from the ECAL measurement with a procedure described in greater detail in Section 5.1. The energy of electrons is determined from a combination of the electron momentum at the primary interaction vertex as determined by the tracker, the energy of the corresponding ECAL cluster, and the energy sum of all bremsstrahlung photons spatially compatible with originating from the electron track. The energy of muons is obtained from the curvature of the corresponding track. The energy of charged hadrons is determined from a combination of their momentum measured in the tracker and the matching ECAL and HCAL energy deposits, corrected for zero-suppression effects and for the response function of the calorimeters to hadronic showers. Finally, the energy of neutral hadrons is obtained from the corresponding corrected ECAL and HCAL energy.

Hadronic jets are clustered from these reconstructed particles using the infrared- and collinear-safe anti- k_T algorithm [20], with a distance parameter of 0.4. The jet momentum is determined as the vectorial sum of all particle momenta in the jet. An offset correction is applied to jet energies to take into account the contribution from additional proton-proton interactions within the same or nearby bunch crossings. Jet energy corrections are derived from simulation, and are confirmed with in situ measurements of the energy balance in dijet, multijet, photon + jet, and leptonically decaying Z + jets events [21]. The jet momentum is found from simulation to be within 5 to 10% of the true momentum over the entire jet transverse momentum (p_T) spectrum and detector acceptance. Additional selection criteria are applied to each event to remove spurious jet-like features originating from isolated noise patterns in certain HCAL regions.

To identify jets originating from the hadronization of bottom quarks, the combined secondary vertex (CSV) b tagging algorithm is used [22, 23]. The algorithm tags jets from b hadron decays by their displaced decay vertex, providing a numerical discriminant value that is higher for jets likely to be initiated by b quarks. Two tagging algorithm working points, medium and loose, are used in this analysis: the medium (loose) point provides an efficiency for identifying b quark jets of about 70% (85%) and a misidentification probability for jets from light quarks and gluons of about 1% (10%).

The missing transverse momentum vector is taken as the negative vector sum of all reconstructed particle candidate transverse momenta in the event reconstruction, and its magnitude is referred to as p_T^{miss} .

A more detailed description of the CMS detector, together with a definition of the coordinate system used and the relevant kinematic variables, can be found in Ref. [24].

3 Analysis strategy

The dominant Higgs boson production mechanism in proton-proton collisions is gluon-gluon fusion (ggH), with additional contributions from vector boson fusion (VBF), and production in association with a vector boson (VH) or with a top quark pair ($t\bar{t}H$).

To maximise the sensitivity of the analysis, specific production modes with reduced background contamination are targeted. Events are categorized by requiring specific features in the final state: forward jets for VBF, top decay products such as muons, electrons, missing transverse energy from neutrinos, jets arising from the hadronization of b quarks for $t\bar{t}H$, and

vector-boson decay products such as muons, electrons, missing transverse energy, or dijets with a characteristic invariant mass for VH production. The events with no specific features, mostly coming from ggH, are categorized according to their expected probability to be signal rather than background.

Several multivariate techniques are used in the analysis. An initial set is used to improve the event reconstruction, and particularly the photon energy estimate, the photon identification, the identification of the diphoton primary vertex and the estimate of its probability of being the true diphoton vertex. In the subsequent steps of the analysis, the event classification benefits from multivariate techniques to categorize ggH events, to enhance the identification of forward jets in VBF events and the separation of such events from ggH events, to enhance the b tagging and the separation of ttH jets in events with multiple jets.

Measurements are extracted by a simultaneous maximum-likelihood fit to the diphoton invariant mass distributions in all event categories. Simulated samples are used to derive the signal model, while the background is obtained from the fit to the data. The latter aspect is particularly important, as it makes the use of simulated samples only relevant to the optimization of the multivariate classifiers used in the different steps of the analysis. While imperfect simulation might induce suboptimal performance, the use of multivariate inputs uncorrelated with the diphoton invariant mass ensures that no bias is introduced. The impact of the choice of the event generator on the multivariate discriminators has also been checked and found to be negligible.

4 Data sample and simulated events

The events used in this analysis were selected by diphoton triggers with asymmetric transverse energy (E_T) thresholds of 30 and 18 GeV. The trigger selection requires a loose calorimetric identification using the shape of the electromagnetic showers, a loose isolation requirement, and a selection on the ratio of the HCAL and ECAL deposits of the photon candidates. The R_9 shower shape variable is used in the trigger to identify photons that convert to an e^+e^- pair in the tracker material before reaching the ECAL surface. The R_9 variable is defined as the energy sum of the 3×3 crystals centred on the most energetic crystal in the candidate electromagnetic cluster divided by the energy of the candidate. The electromagnetic showers from photons that convert before reaching the calorimeter have wider transverse profiles and lower values of R_9 than those of unconverted photons. The trigger efficiency is measured from $Z \rightarrow e^+e^-$ events using the tag-and-probe technique [25]. Efficiencies in simulation are corrected to match those measured in data.

Simulated signal events are generated using MADGRAPH5_aMC@NLO v2.2.2 at next-to-leading order (NLO) [26] in perturbative quantum chromodynamics (QCD) with FxFx merging [27], the parton level samples being interfaced to PYTHIA8.205 [28] for parton showering and hadronization. The CUETP8M1 PYTHIA underlying event tune parameter set is used [29]. Events produced via the gluon fusion mechanism are weighted as a function of the Higgs boson p_T and the number of jets in the event, to match the prediction from the NNLOPS program [30]. Parton distribution functions (PDFs) are taken from the NNPDF3.0 [31] set. The signal cross sections and branching fraction recommended by the LHC Higgs cross section working group are used [32].

The dominant background to $H \rightarrow \gamma\gamma$ consists of the irreducible prompt diphoton production, and the reducible backgrounds from $\gamma + \text{jet}$ and dijet events where the jets are misidentified as isolated photons. Background events, used for the trainings of multivariate discriminants and

for category optimization, have been simulated using various event generators. The diphoton background is modeled with the SHERPA v.2.2.1 [33] generator. It includes the Born processes with up to 3 additional jets as well as the box processes at leading order. Multijet and $\gamma + \text{jet}$ backgrounds are modeled with PYTHIA, with a filter applied to enhance the production of jets with a large fraction of electromagnetic energy. The $W\gamma$ and $Z\gamma$ samples are generated with MADGRAPH5_aMC@NLO at leading order, while Drell–Yan events are simulated with the same generator at NLO precision.

The detailed response of the CMS detector is simulated using the GEANT4 [34] package. This includes the simulation of the multiple proton-proton interactions taking place in each bunch crossing, referred to as pileup. These can occur at the nominal bunch crossing (in-time pileup) or at the crossing of previous and subsequent bunches (out-of-time pileup), and the simulation accounts for both. Simulated events are weighted to reproduce the distribution of the number of interactions in data. The average number of pileup interactions measured in data amounts to 23, with a root-mean-square (RMS) of about 6.

5 Photon reconstruction and identification

Photon candidates are reconstructed as part of the global event reconstruction, as described in Section 2. Photons are identified as ECAL energy clusters not linked to the extrapolation of any charged-particle trajectory to the ECAL. The clustering algorithm allows an almost complete collection of the energy of the photons, even for those converting in the material upstream of the calorimeter. First, cluster “seeds” are identified as local energy maxima above a given threshold. Second, clusters are grown from the seeds by aggregating crystals with at least one side in common with a clustered crystal and with an energy in excess of a given threshold. This threshold represents about two standard deviations of the electronic noise in the ECAL and amounts to 80 MeV in the barrel and, depending on $|\eta|$, up to 300 MeV in the endcaps. The energy of each crystal can be shared among adjacent clusters assuming a Gaussian transverse profile of the electromagnetic shower. Finally, clusters are merged into “superclusters”, to allow good energy containment, accounting for geometrical variations of the detector along η , and optimizing robustness against pileup.

5.1 Photon energy

The energy of photons is computed from the sum of the energy of the clustered crystals, calibrated and corrected for changes in the response over time [18] and considered in the clustering procedure. The preshower energy is added to that of the superclusters in the region covered by this detector. To optimize the resolution, the photon energy is corrected for the containment of the electromagnetic shower in the superclusters and the energy losses from converted photons [35]. The correction is computed with a multivariate regression technique that estimates simultaneously the energy of the photon and its uncertainty. This regression is trained on simulated photons using as the target the ratio of the true photon energy and the sum of the energy of the clustered crystals. The inputs are shower shapes and position variables – both sensitive to shower containment and possible unclustered energy – preshower information, and global event observables sensitive to pileup.

A multistep procedure has been implemented to correct the energy scale in data, and to determine the additional smearing to be applied to the reconstructed photon energy in simulated events so as to reproduce the energy resolution observed in data. First, the energy scale in data is equalized with that in simulated events, and residual long-term drifts in the response are corrected, using $Z \rightarrow e^+e^-$ decays in which the electron showers are reconstructed as pho-

tons. Then, the photon energy resolution predicted by the simulation is improved by adding a Gaussian smearing determined from the comparison between the $Z \rightarrow e^+e^-$ line-shape in data and simulation (Fig. 1). The corrections to the energy scale are extracted differentially in time, $|\eta|$ (two categories in the barrel and two in the endcaps) and R_9 (two categories). They range from about 0.1 to about 0.3% in the barrel and from about 0.2 to about 2% in the endcap, depending on the category. The amount of smearing required is extracted differentially in the same $|\eta|$ and R_9 categories as the energy scale corrections and ranges from about 0.1 to about 2.7%, depending on the category.

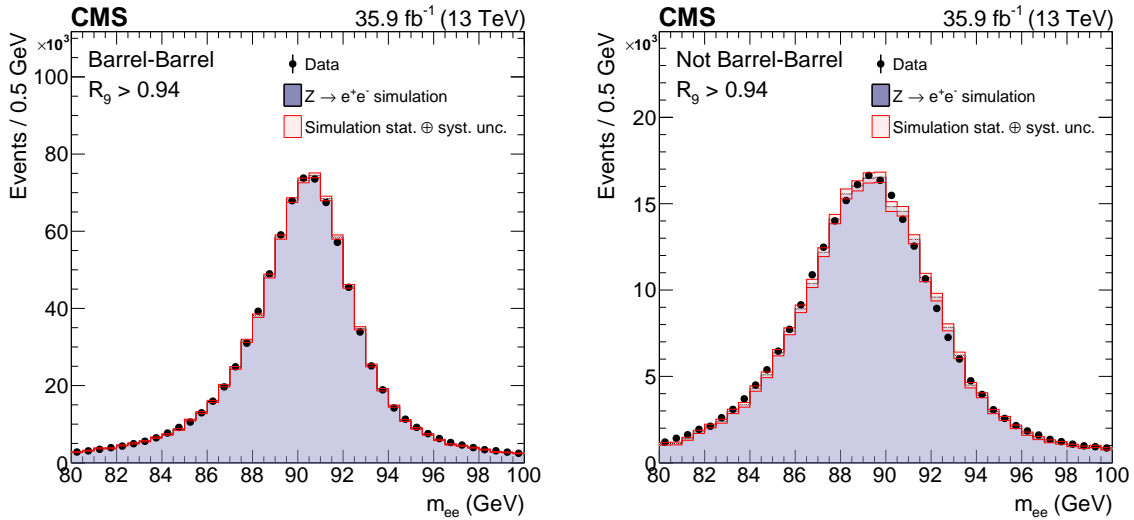


Figure 1: Comparison of the dielectron invariant mass distributions in data and simulation (after energy smearing) for $Z \rightarrow e^+e^-$ events where electrons are reconstructed as photons. The comparison is shown requiring $R_9 > 0.94$ for both “photons” and for (left) events with both photons in the barrel, and (right) the remaining events. The simulated distributions are normalized to the integral of the data distribution in the range $87 < m_{ee} < 93$ GeV to highlight the agreement in the bulk of the distributions.

5.2 Photon preselection

The photons considered further in this analysis are required to satisfy preselection criteria similar to, but slightly more stringent than, the trigger requirements. The preselection requirements consist of:

- $p_T^{\gamma 1} > 30$ GeV and $p_T^{\gamma 2} > 20$ GeV, where $p_T^{\gamma 1}$ and $p_T^{\gamma 2}$ are the transverse momenta of the leading (in p_T) and subleading photons, respectively;
- $|\eta| < 2.5$, excluding the barrel-endcap transition region $1.44 < |\eta| < 1.57$, where the photon energy reconstruction is affected by a suboptimal containment of the electromagnetic shower;
- a selection on the R_9 variable and on $\sigma_{\eta\eta}$ – the lateral extension of the shower, defined as the energy-weighted spread within the 5×5 crystal matrix centred on the crystal with the largest energy deposit in the supercluster – to reject ECAL energy deposits incompatible with a single isolated electromagnetic shower, such as those coming from neutral mesons;
- a selection on the ratio of the energy in the HCAL cells behind the supercluster to the energy in the supercluster (H/E), to reject hadrons;

- an electron veto, which rejects the photon candidate if its supercluster is matched to an electron track with no missing hits in the innermost tracker layers;
- a requirement on the photon isolation (\mathcal{I}_{ph}), defined as the sum of the transverse energy of the particles identified as photons and falling inside a cone of radius $R = \sqrt{(\Delta\eta)^2 + (\Delta\phi)^2} = 0.3$ around the photon candidate direction; the sum is corrected for the contribution of the pileup estimated from the median energy density in the event [36];
- a requirement on the track isolation in a hollow cone (\mathcal{I}_{tk}), the sum of the transverse momenta of all tracks in a cone of radius $R = 0.3$ around the photon candidate direction (with tracks in an inner cone of size $R = 0.04$ not included in the sum); the cone is hollow to use the same isolation definition also for electrons;
- a loose requirement on charged-hadron isolation (\mathcal{I}_{ch}), the sum of the transverse momenta of charged particles inside a cone of radius $R = 0.3$ around the photon candidate; this requirement is added to the one on track isolation to match the selection applied to photon candidates as part of data reconstruction;
- a loose requirement on the photon identification (as described in Section 5.3).

The selection thresholds are reported in Table 1. Additionally, both photons must satisfy either (a) $R_9 > 0.8$ and $\mathcal{I}_{\text{ch}} < 20 \text{ GeV}$, or (b) $\mathcal{I}_{\text{ch}}/p_{\text{T}}^\gamma < 0.3$.

Table 1: Schema of the photon preselection requirements.

	R_9	H/E	$\sigma_{\eta\eta}$	\mathcal{I}_{ph} (GeV)	\mathcal{I}_{tk} (GeV)
Barrel	[0.5, 0.85]	<0.08	<0.015	<4.0	<6.0
	>0.85	<0.08	—	—	—
Endcaps	[0.8, 0.90]	<0.08	<0.035	<4.0	<6.0
	>0.90	<0.08	—	—	—

The efficiency of all preselection criteria, except the electron veto requirement, is measured with a tag-and-probe technique using $Z \rightarrow e^+e^-$ events. The efficiency for photons to satisfy the electron veto requirement, which cannot be measured with $Z \rightarrow e^+e^-$ events, is obtained from $Z \rightarrow \mu^+\mu^-\gamma$ events, in which the photon is produced by final-state radiation and provides a sample of prompt photons with a purity higher than 99%. The photon p_{T} in this sample ranges from about 20 to about 60 GeV. The measured efficiency for photons to satisfy the electron veto requirement has no dependency on the photon p_{T} within about $\pm 1\%$, and is well reproduced in simulated events.

Table 2 shows the preselection efficiencies measured in data, ϵ_{data} , and simulation, ϵ_{MC} , along with their ratio $\epsilon_{\text{data}}/\epsilon_{\text{MC}}$. Statistical and systematic uncertainties are included both in the efficiencies and in their ratio. The measured ratios are used to correct the signal efficiency in simulated signal samples and the associated uncertainties are propagated to the expected signal yields.

5.3 Photon identification

A boosted decision tree (BDT) is used to separate prompt photons from photon candidates that arise from misidentified jet fragments, but which satisfy the preselection. This photon identification BDT is trained using simulated $\gamma + \text{jet}$ events where prompt photons are considered as signal and non-prompt photons as background.

The photon identification BDT is trained with the following input variables:

Table 2: Photon preselection efficiencies as measured in four photon categories, obtained with tag-and-probe techniques using $Z \rightarrow e^+e^-$ and $Z \rightarrow \mu^+\mu^-\gamma$ events. The quoted uncertainties include the statistical and systematic components.

Preselection category	ϵ_{data} (%)	ϵ_{MC} (%)	$\epsilon_{\text{data}}/\epsilon_{\text{MC}}$
Barrel; $R_9 > 0.85$	94.2 ± 0.9	94.7 ± 0.9	0.995 ± 0.001
Barrel; $R_9 < 0.85$	82.5 ± 0.7	82.5 ± 0.7	1.000 ± 0.003
Endcap; $R_9 > 0.90$	90.1 ± 0.2	91.3 ± 0.1	0.987 ± 0.005
Endcap; $R_9 < 0.90$	49.7 ± 1.4	53.8 ± 1.5	0.923 ± 0.010

- shower shape observables, corrected to mitigate data and simulation discrepancies;
- isolation variables, \mathcal{I}_{ph} and \mathcal{I}_{ch} ; two kinds of \mathcal{I}_{ch} are computed, including hadrons associated with the chosen primary vertex (described in Section 6), and including hadrons associated with the vertex providing the largest isolation sum; the latter is effective in rejecting misidentified photon candidates originating from jets coming from a vertex other than the chosen one;
- photon η and energy, which are correlated with the shower topology and isolation variables;
- the median energy density per unit area in the event, ρ , to minimize the impact of pileup on the above inputs.

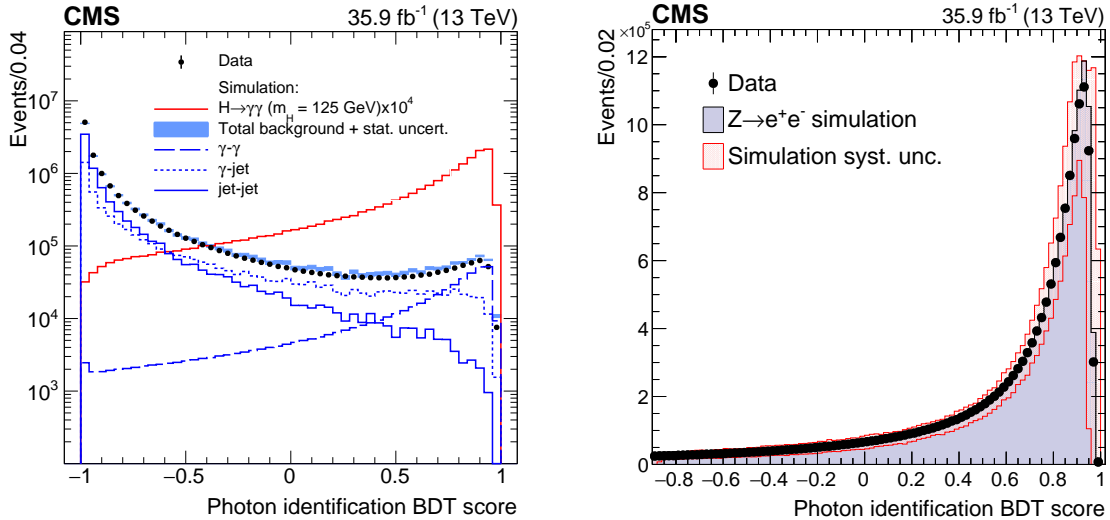


Figure 2: (Left) Distribution of the photon identification BDT score of the lowest scoring photon of diphoton pairs with an invariant mass in the range $100 < m_{\gamma\gamma} < 180$ GeV, for events passing the preselection in the 13 TeV data set (points), and for simulated background events (blue histogram). Histograms are also shown for different components of the simulated background. The sum of all background distributions is scaled up to data. The red histogram corresponds to simulated Higgs boson signal events. (Right) Distribution of the photon identification BDT score for $Z \rightarrow e^+e^-$ events in data and simulation, where the electrons are reconstructed as photons. The systematic uncertainty applied to the shape from simulation (hashed region) is also shown.

Figure 2 (left) shows the photon identification BDT score of the lowest-scoring photon from all diphoton pairs with an invariant mass in the range $100 < m_{\gamma\gamma} < 180$ GeV, for events passing the preselection in data and simulated background events.

The photon identification BDT score is also shown in Fig. 2 (right) for electrons reconstructed as photons in $Z \rightarrow e^+e^-$ events, in data and simulation. The systematic uncertainty in the photon identification score, represented by the hashed region, is conservatively assigned to cover the largest observed discrepancy between data and simulation for electrons in the ECAL endcaps.

6 Diphoton vertex

The determination of the primary vertex from which the two photons originate has a direct impact on the diphoton invariant mass resolution. If the position along the beam axis (z) of the interaction producing the diphoton is known to better than about 10 mm, the invariant mass resolution is dominated by the photon energy resolution. For comparison, the distribution in z of the position of the vertices reconstructed from the observed tracks has an RMS spread of about 3.4 cm.

The diphoton vertex assignment relies on a BDT (the vertex identification BDT) whose inputs are observables related to tracks recoiling against the diphoton system:

- $\sum_i |\vec{p}_T^i|^2$,
- $-\sum_i \vec{p}_T^i \cdot \vec{p}_T^{\gamma\gamma} / |\vec{p}_T^{\gamma\gamma}|$,
- $(|\sum_i \vec{p}_T^i| - p_T^{\gamma\gamma}) / (|\sum_i \vec{p}_T^i| + p_T^{\gamma\gamma})$,

where \vec{p}_T^i is the transverse momentum of the i th track associated with a given vertex and $\vec{p}_T^{\gamma\gamma}$ is the transverse momentum of the diphoton system measured with respect to the same vertex. The sum runs over all charged particle-flow candidates associated with the given vertex.

In the presence of tracks from photons converted in the tracker material, two additional input variables are used:

- the number of conversions,
- the pull $|z_{\text{vtx}} - z_e| / \sigma_z$ between the longitudinal position of the reconstructed vertex, z_{vtx} , and the longitudinal position of the vertex estimated using conversion track(s), z_e , where the variable σ_z denotes the uncertainty in z_e .

A second vertex-related multivariate discriminant (vertex probability BDT), used in the diphoton BDT (discussed in Section 7), is designed to estimate, event-by-event, the probability for the vertex assignment to be within 10 mm of the diphoton interaction point. The vertex probability BDT is trained on simulated $H \rightarrow \gamma\gamma$ events using the following input variables:

- the number of vertices in each event;
- the values of the vertex identification BDT score for the three most probable vertices in each event;
- the distances between the chosen vertex and the second and third choices;
- the magnitude of the transverse momentum of the diphoton system, $p_T^{\gamma\gamma}$;
- the number of photons with an associated conversion track.

The performance of the vertex identification BDT is validated using $Z \rightarrow \mu^+\mu^-$ events (Fig. 3), where the vertices are fitted omitting the muon tracks to mimic a diphoton system. In addition, the use of tracks from converted photons to locate the vertex is validated using $\gamma + \text{jet}$ events. Discrepancies between data and simulation are corrected for in the analysis and a corresponding uncertainty is considered.

In the simulated samples the width of the beam spot was about a factor 1.5 larger than what

was subsequently observed in data. To correct for this, simulated events in which the selected vertex is more than 1 mm away from the generated one are weighted such that the width of the distribution of the primary vertices is the same as the beam spot width in data.

The efficiency of correctly assigning the diphoton vertex to be within 10 mm of the true vertex in $H \rightarrow \gamma\gamma$ simulated events is shown in Fig. 4 as a function of the p_T of the diphoton pair and as a function of the number of primary vertices in the event, and compared with the average estimated vertex probability BDT. The overall efficiency is about 81%.

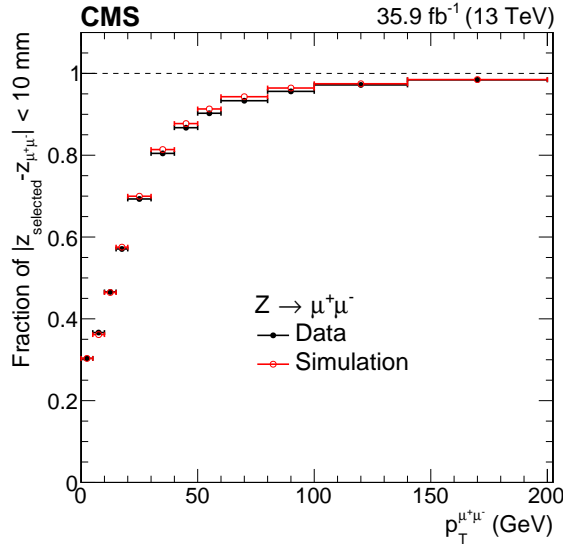


Figure 3: Validation of the $H \rightarrow \gamma\gamma$ vertex identification algorithm on $Z \rightarrow \mu^+\mu^-$ events omitting the muon tracks. Simulated events are weighted to match the distributions of pileup and location of primary vertices in data.

7 Event classification

The event selection requires two preselected photon candidates with $p_T^{\gamma 1} > m_{\gamma\gamma}/3$ and $p_T^{\gamma 2} > m_{\gamma\gamma}/4$, in the mass range $100 < m_{\gamma\gamma} < 180$ GeV. The use of p_T thresholds scaled by $m_{\gamma\gamma}$ prevents a distortion of the low end of the invariant mass spectrum. The requirement on the photon p_T is applied after the vertex assignment.

To improve the sensitivity of the analysis, events are classified targeting different production mechanisms and according to their mass resolution and predicted signal-to-background ratio. In each category, the selections are optimized to maximize the significance of the expected signal with respect to the background. As the first step of the classification, exclusive event categories are defined by dedicated selections on additional reconstructed objects to select Higgs boson production mechanisms other than ggH: VBF, VH or ttH.

All objects are reconstructed as described in Section 2 and (for photons) Section 5. In addition, electrons are required to be within $|\eta| < 2.5$ and outside the barrel-endcap transition region. Muons are required to be within $|\eta| < 2.4$.

A dedicated diphoton BDT is used in the event categorization. The diphoton BDT assigns a high score to events with photons showing signal-like kinematics, good mass resolution, and high photon identification BDT score. The input variables to the classifier are:

- $p_T^\gamma/m_{\gamma\gamma}$ for each photon;

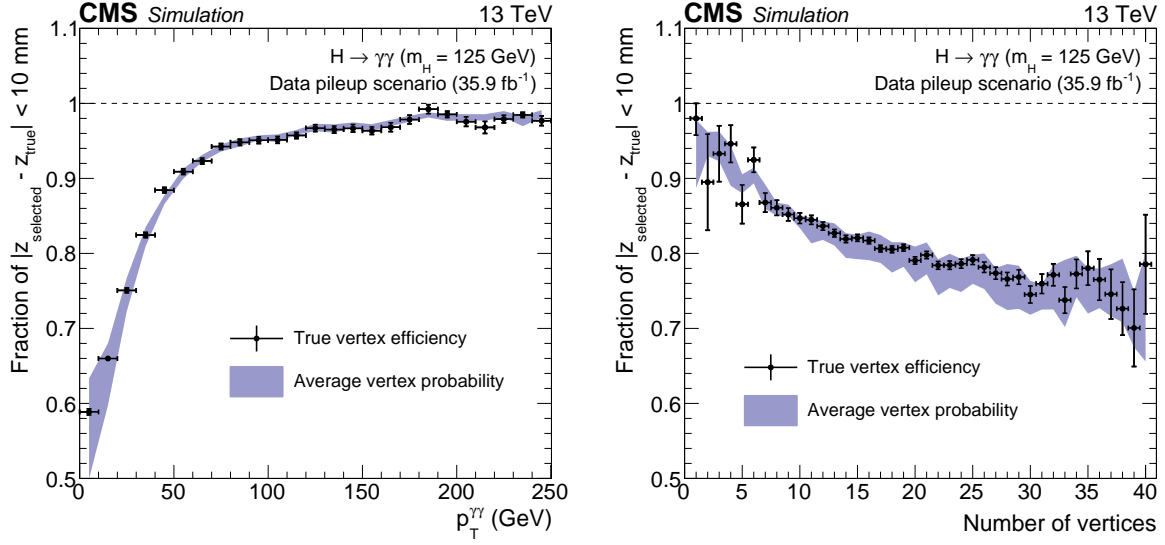


Figure 4: Comparison of the true vertex identification efficiency and the average estimated vertex probability as a function of the reconstructed diphoton p_T (left) and of the number of primary vertices (right) in simulated $H \rightarrow \gamma\gamma$ events with $m_H = 125 \text{ GeV}$. Events are weighted according to the cross sections of the different production modes and to match the distributions of pileup and location of primary vertices in data.

- the pseudorapidity of the two photons;
- the cosine of the angle between the two photons in the transverse plane;
- photon identification BDT scores for both photons;
- two per-event relative mass resolution estimates, one under the hypothesis that the mass has been reconstructed using the correct primary vertex, and the other under the hypothesis that the mass has been reconstructed using an incorrect vertex;
- the per-event probability estimate that the correct primary vertex has been assigned to the diphoton.

The relative mass resolution is computed from the propagation of the photon energy resolution estimates, assuming the functional forms of the photon resolutions are Gaussian. Figure 5 (left) shows the transformed score from the diphoton multivariate classifier for data and simulated signal and backgrounds, for events with two photons satisfying the preselection requirements. The classifier score has been transformed such that the sum of signal events from all the production modes has a uniform distribution. A validation of the score from the diphoton multivariate classifier obtained in $Z \rightarrow e^+e^-$ events, where the electrons are reconstructed as photons, is shown in Fig. 5 (right) for data and simulation.

7.1 Event categories for $t\bar{t}H$ production

Events produced in association with a top quark pair feature two b quarks from the decay of the top quarks, and may be accompanied by charged leptons or additional jets. In the latter case, to enhance the tagging of $t\bar{t}H$ multijet events, a multivariate discriminant is built upon the following inputs:

- the number of jets with $p_T > 25 \text{ GeV}$;
- the leading jet p_T ;

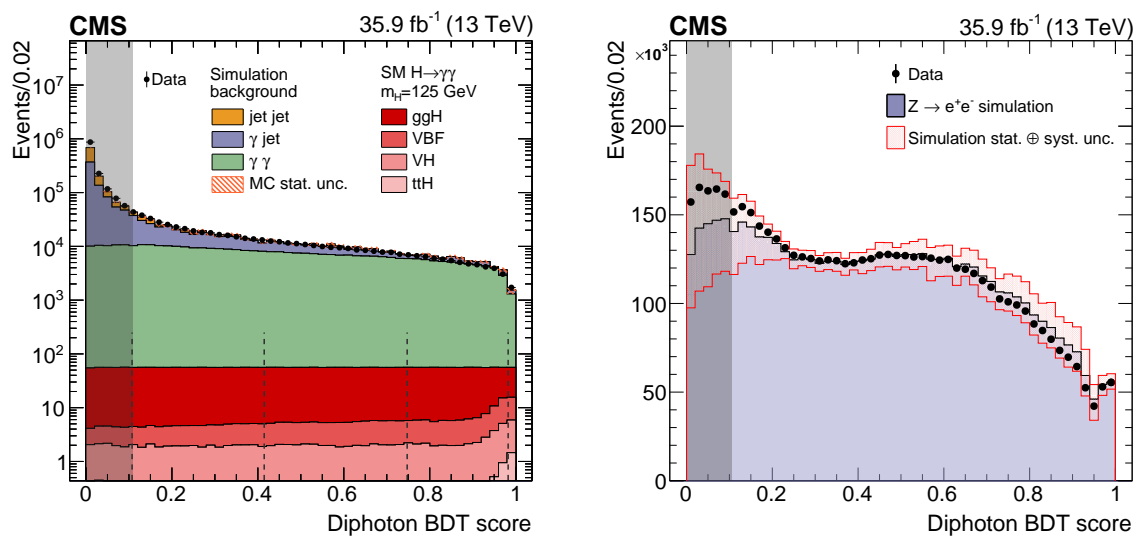


Figure 5: (Left) Transformed score distribution from the diphoton multivariate classifier for events with two photons satisfying the preselection requirements in data (points), simulated signal (red shades), and simulated background (coloured histograms). Both signal and background are stacked together. The vertical dashed lines show the boundaries of the untagged categories, the grey shade indicates events discarded from the analysis. (Right) Score distribution of the diphoton multivariate classifier in $Z \rightarrow e^+e^-$ events where the electrons are reconstructed as photons. The points show the distribution for data, the histogram shows the distribution for simulated Drell–Yan events. The pink band indicates the statistical and systematic uncertainties in simulation. The grey shade indicates events discarded from the analysis.

- the two highest scores from the btag CSV discriminator.

The output of this discriminant is shown in Fig. 6. The threshold on the discriminant is optimized jointly with the requirement on the diphoton BDT score by maximizing the expected sensitivity to $t\bar{t}H$ production.

To cross-check the performance of this BDT observable, a control sample in data is defined by selecting events with a pair of photons, one of which passes the preselection and photon identification requirements, while the other has no preselection applied and an inverted criterion on the score from the photon identification BDT. As the efficiency for selecting such photons is not the same as for the signal region, events in the control samples are weighted according to the η and p_T of the photons so as to obtain a control sample with similar kinematic properties as the signal region, but statistically independent.

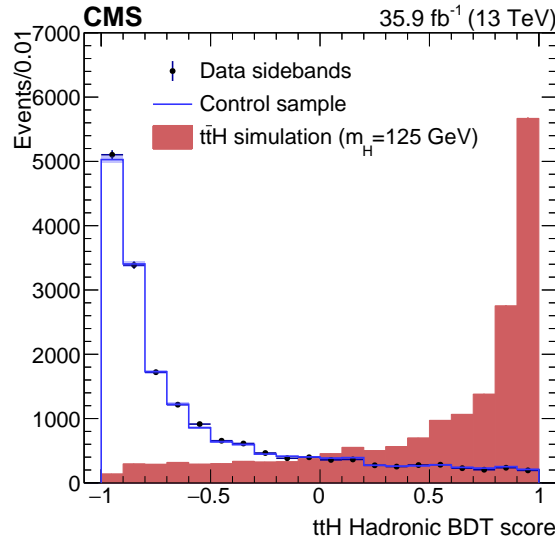


Figure 6: Score distribution of the jet multivariate discriminant used to enhance jet tagging in the $t\bar{t}H$ multijet category. The points show the distribution for data in the signal region sidebands, $m_{\gamma\gamma} < 115 \text{ GeV}$ or $m_{\gamma\gamma} > 135 \text{ GeV}$; the histogram shows the distribution for events in the data control sample; the filled histogram shows the distribution for simulated signal events. The distributions in the simulated and control samples are scaled as to match the integral of that from the data sidebands.

Depending on the type of the top quark decay, the following categories are defined:

- semileptonic top quark decays ($t\bar{t}H$ Leptonic):
 - leading photon $p_T > m_{\gamma\gamma}/2$, subleading photon $p_T > m_{\gamma\gamma}/4$;
 - diphoton classifier BDT score greater than 0.11;
 - at least one lepton with $p_T > 20 \text{ GeV}$; electrons must satisfy loose requirements on the same observables as described in Ref. [37]; muons are required to pass a tight selection based on the quality of the track, the number of hits in the tracker and muon system, and the longitudinal and transverse impact parameters of the track with respect to the muon vertex, and to satisfy a requirement on the relative isolation (after correction for pileup) based on transverse energy of the charged hadrons, neutral hadrons, and photons, in a cone around the muon with a radius between 0.05 and 0.2, depending on the p_T of the muon;

- all selected leptons ℓ are required to have $R(\ell, \gamma) > 0.35$, where R is the distance between the objects in the $\eta - \phi$ plane;
- specifically for electrons: $|m_{e,\gamma} - m_Z| > 5 \text{ GeV}$, where $m_{e,\gamma}$ is the invariant mass of any pair of electron and photon and m_Z refers to the mass of the Z boson;
- at least two jets in the event with $p_T > 25 \text{ GeV}$, $|\eta| < 2.4$, and $R(\text{jet}, \gamma) > 0.4$ and $R(\text{jet}, \ell) > 0.4$;
- at least one of the jets in the event identified as a b jet according to the CSV tagger medium requirement;
- hadronic top quark decays (ttH Hadronic):
 - leading photon $p_T > m_{\gamma\gamma}/3$, subleading photon $p_T > m_{\gamma\gamma}/4$;
 - diphoton classifier BDT score greater than 0.58;
 - no leptons, defined according to the criteria of the ttH Leptonic category;
 - at least three jets in the event with $p_T > 25 \text{ GeV}$ and $|\eta| < 2.4$;
 - at least one of the jets in the event identified as a b jet according to the CSV tagger loose requirement;
 - score from the ttH Hadronic multivariate discriminant greater than 0.75.

7.2 Event categories for VH production

The selection criteria targeting the associated production of the Higgs boson with a vector W or Z boson exploit the presence of leptons, missing transverse momentum, and jets. To reduce contamination from Drell–Yan events with an electron misreconstructed as a photon, or with photons radiated in the final state, photon candidates are required to be separated in angle from the closest lepton. The criteria are the following:

- leptonic Z decays (ZH Leptonic):
 - leading photon $p_T > 3m_{\gamma\gamma}/8$, subleading photon $p_T > m_{\gamma\gamma}/4$;
 - diphoton classifier BDT score greater than 0.11;
 - two same-flavour leptons within the fiducial region, $p_T > 20 \text{ GeV}$; electrons and muons are required to satisfy the same identification criteria as for the ttH Leptonic category;
 - dilepton invariant mass $m_{\ell\ell}$ in the range $70 < m_{\ell\ell} < 110 \text{ GeV}$;
 - $R(\gamma, e) > 1.0$, $R(\gamma, \mu) > 0.5$, for each of the leptons;
 - in addition, a conversion veto is applied to the electrons to reduce the number of electrons originating from photon conversions, by requiring that, when an electron and a photon candidate share a supercluster, the electron track is well separated from the centre of the supercluster:
 $R(\text{supercluster}, e\text{-track}) > 0.4$.
- leptonic W decays (WH Leptonic):
 - leading photon $p_T > 3m_{\gamma\gamma}/8$, subleading photon $p_T > m_{\gamma\gamma}/4$;
 - diphoton classifier BDT score greater than 0.28;
 - at least one lepton with $p_T > 20 \text{ GeV}$; electrons and muons are required to satisfy the same identification criteria as for the ZH Leptonic category;
 - $R(\gamma, \ell) > 1.0$ and conversion veto as in the ZH Leptonic category;
 - missing transverse momentum $p_T^{\text{miss}} > 45 \text{ GeV}$;
 - up to two jets each satisfying $p_T > 20 \text{ GeV}$, $|\eta| < 2.4$, $R(\text{jet}, \ell) > 0.4$, and

$$R(\text{jet}, \gamma) > 0.4;$$

- W or Z leptonic decays, relaxed selection (VH LeptonicLoose):
 - as for WH Leptonic with the requirement on the missing transverse momentum to be $p_T^{\text{miss}} < 45 \text{ GeV}$;
- W or Z leptonic decays, with at least one missing lepton (VH MET):
 - leading photon $p_T > 3m_{\gamma\gamma}/8$, subleading photon $p_T > m_{\gamma\gamma}/4$;
 - diphoton classifier BDT score greater than 0.79;
 - missing transverse momentum $p_T^{\text{miss}} > 85 \text{ GeV}$;
 - angle in the transverse plane between the direction of the diphoton and the \vec{p}_T^{miss} $\Delta\phi(\gamma\gamma, \vec{p}_T^{\text{miss}}) > 2.4$;
- hadronic decays of W and Z (VH Hadronic):
 - leading photon $p_T > m_{\gamma\gamma}/2$, subleading photon $p_T > m_{\gamma\gamma}/4$;
 - diphoton classifier BDT score greater than 0.79;
 - at least two jets, each with $p_T > 40 \text{ GeV}$ and $|\eta| < 2.4$, $R(\text{jet}, \gamma) > 0.4$;
 - dijet invariant mass in the range $60 < m_{jj} < 120 \text{ GeV}$;
 - $|\cos\theta^*| < 0.5$, where θ^* is the angle that the diphoton system makes, in the diphoton-dijet centre-of-mass frame, with respect to the direction of motion of the diphoton-dijet system in the lab frame. The distribution of this variable is rather uniform for VH events, while it is strongly peaked at 1 for background and events from ggH production.

7.3 Event categories for VBF production

Events produced via the VBF process feature two jets in the final state separated by a large rapidity gap. A multivariate discriminant is trained to tag the distinctive kinematics of the VBF jets, considering as background the production process of ggH + jets. This discriminant is given as input to an additional multivariate classifier (VBF combined BDT) along with the score from the diphoton BDT, and the ratio $p_T^{\gamma\gamma}/m_{\gamma\gamma}$. Figure 7 (left) shows the transformed score from the VBF combined BDT for data in the mass sideband regions from 105–115 GeV and 135–145 GeV, along with the predicted VBF and ggH distributions. The VBF combined BDT score has been transformed such that the signal events from the VBF production mode has a uniform distribution. A validation of the score from the combined multivariate classifier obtained in $Z \rightarrow e^+e^- + \text{jets}$ events, where the electrons are reconstructed as photons and at least two jets satisfy the requirements listed below to enter the VBF category, is shown in Fig. 7 (right) for data and simulation.

The selections targeting the VBF production mechanism are the following:

- leading photon $p_T > m_{\gamma\gamma}/3$, subleading photon $p_T > m_{\gamma\gamma}/4$;
- photon identification BDT score greater than -0.2 , to provide additional rejection against background events whose kinematics yield a high diphoton BDT score despite one reconstructed photon with a relatively low photon identification BDT score;
- one jet with $p_T > 40 \text{ GeV}$ and one with $p_T > 30 \text{ GeV}$, both with $|\eta| < 4.7$ and with a tight requirement on the pileup jet identification;
- invariant mass of the two jets $m_{jj} > 250 \text{ GeV}$;
- VBF combined multivariate discriminant greater than 0.43.

Three categories are defined using the score from the combined discriminant, and are opti-

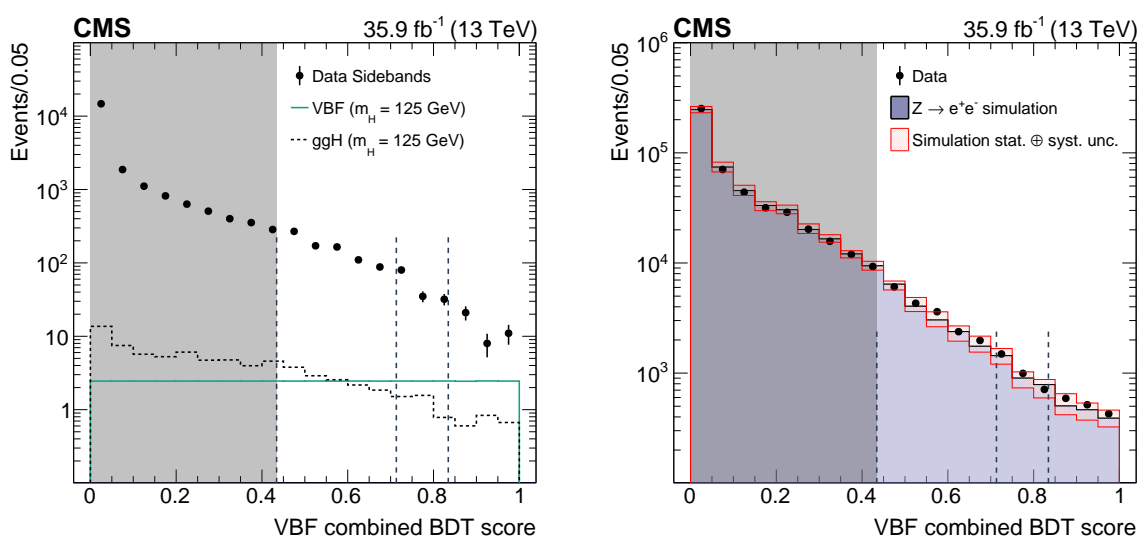


Figure 7: Score distribution from the VBF combined BDT for (left) ggH and VBF signal distributions, compared to background taken from data in the mass sideband regions, and (right) $Z \rightarrow e^+e^- + \text{jets}$ events. On the left, the signal region selection is applied to the simulated ggH and VBF events; these are compared to points representing the background, as determined from data using the signal region selection in mass sidebands. On the right, the signal selection is applied to electrons reconstructed as photons, with points showing the distribution for data and the histogram showing the distribution for simulated Drell–Yan events, including statistical and systematic uncertainties (pink band). In both plots, dotted lines delimit the three VBF categories, while the grey region is discarded from the analysis.

mized to maximize the expected signal significance in the VBF production channel.

7.4 Event categories for ggH production

Events not passing any exclusive category are classified using the multivariate discriminator described in the introduction of this section. The score from this classifier is used to select and divide the events into four “untagged” categories according to the diphoton mass resolution and predicted signal over background ratio. The number of categories is determined by maximizing the expected signal significance. The boundaries of these categories are shown in Fig. 5.

7.5 Final classification

Each event is classified exclusively by applying the category selections in order and choosing the highest-priority category satisfied by the event. Category selections targeting specific production processes are applied first, ranked by expected signal significance, then untagged categories. The final ordering is thus ttH Leptonic, ttH Hadronic, ZH Leptonic, WH Leptonic, VH LeptonicLoose, VBF categories, VH MET, VH Hadronic, and untagged. The fraction of events with multiple diphoton pairs satisfying one or more category selections is less than 2×10^{-4} . In this case, the diphoton in the highest-priority category is selected or, in case of ambiguities, the diphoton pair with the highest sum of photon p_T is selected.

8 Signal model

The signal shape for the diphoton invariant mass distribution in each category and for a nominal Higgs boson mass m_H is constructed from simulation using events from the different production modes.

The simulation includes the tuning of the photon shower variables to the data, and accounts for trigger, reconstruction and identification efficiencies as measured with data-driven techniques (as discussed in Section 5). It also weights the events so that the distribution of the number of interactions and the primary vertex location reproduce those observed in data, as explained in Sections 4 and 6.

Since the shape of the $m_{\gamma\gamma}$ distribution changes considerably depending on whether the vertex associated with the candidate diphoton was correctly identified within 10 mm, distributions for the correct vertex and wrong vertex assignments are fit separately when constructing the signal model. For each process, category, and vertex scenario, the $m_{\gamma\gamma}$ distributions are fitted using a sum of at most five Gaussian functions.

For each process, category, and vertex scenario, a simultaneous fit of signal samples at mass values in the range from 120 to 130 GeV is performed to obtain parametric variations of the Gaussian function parameters used in the signal model fit. Polynomials are used to describe these variations.

The final fit function for each category is obtained by summing the functions for all production modes normalized to the expected signal yields in that category. Figure 8 shows the signal model corresponding to $m_H = 125$ GeV for the best resolution category and also for all categories combined together, weighted by the $S/(S+B)$ ratio, where S is the number of signal events, and B the number of background events in a window around the signal peak, in each category.

The product of efficiency and acceptance of the signal model as a function of m_H for all categories combined is shown in Fig. 9.

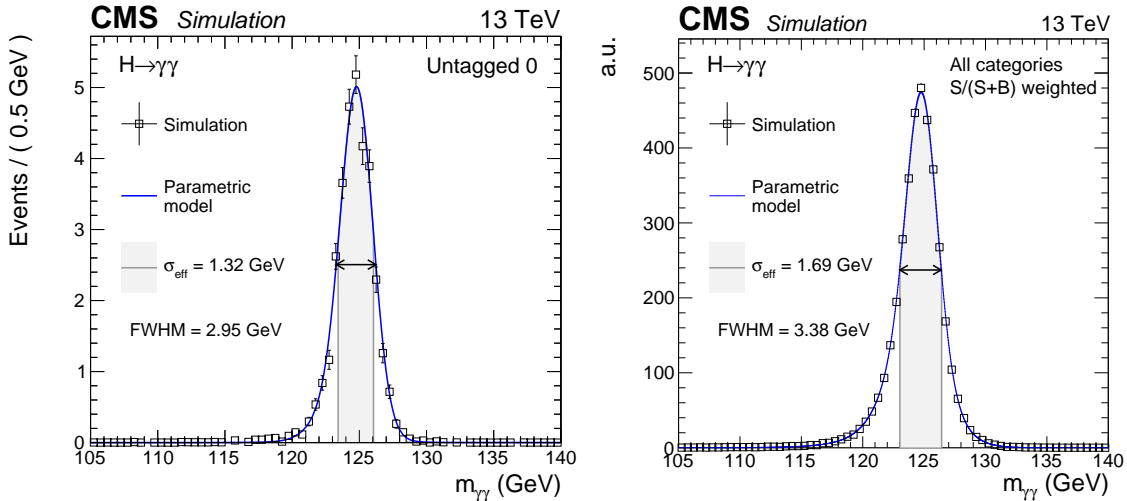


Figure 8: Parametrized signal shape for the best resolution category (left) and for all categories combined together and weighted by the $S/(S+B)$ ratio (right) for a simulated $H \rightarrow \gamma\gamma$ signal sample with $m_H = 125$ GeV. The open squares represent weighted simulated events and the blue lines are the corresponding models. Also shown are the σ_{eff} value (half the width of the narrowest interval containing 68.3% of the invariant mass distribution) and the corresponding interval as a grey band, and the full width at half maximum (FWHM) and the corresponding interval as a double arrow.

9 Background model

The model used to describe the background is extracted from data with the discrete profiling method [38] as implemented in Ref. [15]. This technique was designed as a way to estimate the systematic uncertainty associated with choosing a particular analytic function to fit the background $m_{\gamma\gamma}$ distribution. The method treats the choice of the background function as a discrete nuisance parameter in the likelihood fit to the data.

No assumptions are made about the particular processes composing the background nor the functional form of their smoothly falling diphoton invariant mass distribution. A large set of candidate function families is considered, including exponentials, Bernstein polynomials, Laurent series, and power law functions. For each family of functions, an F-test [39] is performed to determine the maximum order to be used, while the minimum order is determined by requiring a reasonable fit to the data. The background is assumed to be a smoothly falling distribution; this is supported by the shape of background distributions both in simulated events and in data, in the latter case those of the events rejected by the diphoton BDT.

When fitting these functions to the background $m_{\gamma\gamma}$ distribution, the value of twice the negative logarithm of the likelihood (2NLL) is minimized. A penalty of n_p is added to 2NLL to take into account the number of floating parameters n_p in each candidate function and avoid favouring functions with a greater number of free parameters. When making a measurement of a given parameter of interest, the discrete profiling method determines the minimal 2NLL by considering all allowed functions for each value of the parameter.

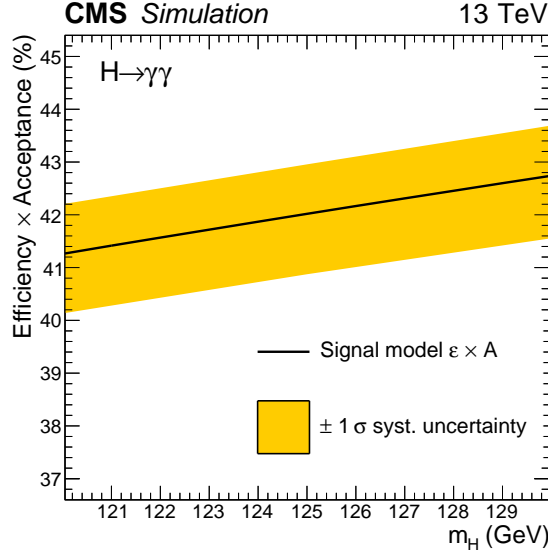


Figure 9: The product of efficiency and acceptance of the signal model as a function of m_H for all categories combined. The black line represents the yield from the signal model. The yellow band indicates the effect of the ± 1 standard deviation of the systematic uncertainties for trigger, photon identification and selection, photon energy scale and modelling of the photon energy resolution, and vertex identification (described in Section 10).

10 Systematic uncertainties

The systematic uncertainties are treated differently depending on how they affect the $m_{\gamma\gamma}$ signal distribution. The parameters of the signal model shape are allowed to vary, within the constraints set by the measurements described in Section 5.1, to account for systematic uncertainties in the photon scale and resolution. Additional nuisance parameters are included to account for systematic uncertainties which affect the overall rate and migration of signal events between the categories, and are log-normal constrained. For cases where the systematic uncertainty has an effect on the input to one of the classification discriminants, the uncertainty takes the form of a variation in the category yield, representing event migration between categories.

10.1 Theoretical uncertainties

Theoretical uncertainties in the signal yield associated with QCD calculations typically have an overall normalization uncertainty, taken from Ref. [32], along with an additional uncertainty accounting for the migration of events between the analysis categories. The category migration uncertainties are factorized from the overall yield uncertainty by scaling them appropriately so that the overall yield (including events outside the acceptance of the analysis) is unchanged. The uncertainties computed in this way are:

- *QCD scale uncertainty*: related to variations of the renormalization and factorization scales, has two nuisance parameters affecting the overall normalization uncertainty and depending on the number of jets in the event. Variations are found to be typically less than 5%.
- *PDF uncertainties*: have an overall normalization from the PDF4LHC prescription [32, 40], while the bin-to-bin migrations are calculated from the NNPDF3.0 [31] PDF set using the MC2HESSIAN procedure [41]. The category migrations are found to be typically less than 1%, depending on the category.

- α_s *uncertainty*: the uncertainty in the value of the strong force coupling constant α_s is evaluated following the PDF4LHC prescription. The overall variation in the relative event yield due to the α_s uncertainty is at most 2.6%.

Further theoretical uncertainties are:

- *Underlying event and parton shower uncertainty*: is obtained using samples where the choice and tuning of the generator has been modified. This systematic uncertainty is treated as an event migration systematic as it will mainly affect the jets in the analysis. The possibility that an event could move from one VBF category to another or from any VBF category to an inclusive category is assigned a systematic uncertainty of 7 and 9%, respectively.
- *Gluon fusion contamination in the $t\bar{t}H$ tagged categories*: the theoretical predictions for gluon fusion are less reliable in a regime where the Higgs boson is produced in association with a large number of jets. The systematic uncertainty in the gluon fusion contamination in the $t\bar{t}H$ tagged categories has been estimated taking into account several contributions:
 - uncertainty due to the limited size of the simulated sample: 10%.
 - uncertainty from the jet modelling. This uncertainty is estimated as the observed difference in the jet multiplicity between MADGRAPH5_aMC@NLO predictions and data in $t\bar{t} + \text{jets}$ events (which are dominated by gluon fusion production $gg \rightarrow t\bar{t}$), with fully leptonic $t\bar{t}$ decays. This uncertainty is about 35% in the bins with the largest discrepancy ($N_{\text{jets}} \geq 5$).
 - uncertainty in the gluon splitting modelling. This is estimated by scaling the fraction of events from gluon fusion with real b jets by the observed difference between data and simulation in the ratio $\sigma(t\bar{t}b\bar{b})/\sigma(t\bar{t}j\bar{j})$ at 13 TeV [42]. This uncertainty implies a variation of about 50% in the yield of gluon fusion events.
- *Gluon fusion contamination in categories with additional jets and a high- p_T Higgs boson*: particularly important for estimating the yield in the VBF categories. A total of seven nuisance parameters account for different systematic effects:
 - uncertainties in jet multiplicities: two nuisance parameters account for missing higher-order corrections and two for migrations between categories with different jet multiplicity. These are based on the STWZ [43] and BLPTW [43–45] predictions.
 - uncertainties in the Higgs boson p_T modelling: two nuisance parameters include migrations between regions with p_T in the range between 60 and 120 GeV and above 120 GeV. A third nuisance parameter accounts for the impact of top quark mass effects, which are negligible for a Higgs boson p_T below 150 GeV and rise to about 35% at 500 GeV; these impact primarily the tightest untagged and VBF categories, where the resulting uncertainty in the predicted gluon fusion yield is 6–8%.
 - uncertainties in the acceptance of gluon fusion events in the VBF categories, due to missing higher-order QCD effects in the calculations: these are estimated by variations of the renormalization and factorization scales in MCFM 5.8 [46]. Two nuisance parameters account for the uncertainty in the overall normalizations of Higgs boson events with 2 extra jets, or with 3 or more extra jets, allowing one to propagate the impact of jet suppression from the kinematic selections in the VBF BDT scores. An exten-

sion of the Stewart–Tackmann method [47, 48] is used. The impact on the yield of gluon fusion events in VBF categories is 8–13%.

- *Uncertainty in the $H \rightarrow \gamma\gamma$ branching fraction*: is estimated to be about 2% [32].

10.2 Experimental uncertainties in the photon energy scale

The experimental uncertainties in the photon energy scale and resolution are propagated through to the signal model in the final statistical fit, allowing the shape to vary. These uncertainties are:

- *Energy scale and resolution*: The uncertainties in the overall photon energy scale and resolution corrections are assessed with $Z \rightarrow e^+e^-$ events and applied to photons. These uncertainties account for varying the R_9 distribution, the regression training (using electrons instead of photons) and the electron selection used to derive the corrections. The uncertainty in the additional energy smearing is assigned propagating the uncertainties in the various $|\eta|$ and R_9 bins to the Higgs boson signal phase space. In both cases dedicated nuisance parameters are included as additional systematic terms in the signal model and amount to a 0.15 to 0.5% effect on the photon energy depending on the photon category. The effect on the measurement of the inclusive signal strength modifier is found to be about 2.5%.
- *Nonlinearity of the photon energy*: An additional uncertainty accounts for the possible residual differences in the linearity of the energy scale between data and simulation. This effect is studied using Lorentz-boosted Z boson dielectron decays. The effect is found to be at most 0.1% on the photon energy in all categories, except in the untagged category with highest signal-to-background ratio, for which it is 0.2%.

Additional uncertainties are assigned based on studies accounting for differences between electrons and photons on the following points.

- *Nonuniformity of the light collection*: The uncertainty in the modelling of the fraction of scintillation light reaching the photodetector as a function of the longitudinal depth in the crystal at which it was emitted. The uncertainty has been slightly increased with respect to Run 1 to account for the larger loss in transparency of the ECAL crystals. The size of the effect on the photon energy scale for 2016 data is estimated to be 0.07%.
- *Electromagnetic shower modelling*: A further small uncertainty is added to account for imperfect electromagnetic shower simulation in GEANT4. A simulation made with a previous version of the shower description, not using the Seltzer–Berger model for the bremsstrahlung energy spectrum [49], changes the energy scale for both electrons and photons. Although mostly consistent with zero, the variation is interpreted as a limitation on our knowledge of the correct simulation of the showers, leading to a further uncertainty of 0.05% in the photon energy.
- *Modelling of the material budget*: The uncertainty in the material budget between the interaction point and the ECAL, which affects the behaviour of electron and photon showers, is estimated with specially simulated samples where the material budget is uniformly varied by $\pm 5\%$. This accounts for the difference in the estimate of the material budget between data and simulation, using methods based on electron bremsstrahlung, multiple scattering of pions, and energy flow in ECAL. The effect on the energy scale is at most 0.24%.
- *Shower shape corrections*: The uncertainty deriving from the imperfect shower shape modelling in simulation. It is estimated using simulation with and without the cor-

rections on the shower shape variables applied to mitigate discrepancies between data and simulation (as described in Section 5.3). This uncertainty in the energy scale is at most 0.01–0.15%, depending on the photon category.

10.3 Additional experimental uncertainties

Other experimental uncertainties are accounted for by propagating the uncertainties in the efficiencies, scale factors, and selection variables through the analysis and applying them to the per-category signal yield:

- *Trigger efficiency*: the trigger efficiency is measured from $Z \rightarrow e^+e^-$ events using the tag-and-probe technique; the impact on the event yields is at most 0.1%.
- *Photon preselection*: the systematic uncertainty is taken as the uncertainty in the ratio between the efficiency measured in data and in simulation; it ranges from 0.1 to 0.7%, according to the photon category, and results in an event yield variation from 0.2 to 0.5%, depending on the event category.
- *Photon identification BDT score*: to cover the observed discrepancies between data and simulation, the uncertainty in the signal yields in the different categories of the analysis is estimated conservatively by propagating the uncertainty described in Section 5 through the diphoton BDT and categorization.
- *Per-photon energy resolution estimate*: this uncertainty is parameterized conservatively as a rescaling of the resolution by $\pm 5\%$ about its nominal value, to cover all differences between data and simulation in the output distribution of the estimator. The variation is propagated through the diphoton BDT and categorization procedure.
- *Jet energy scale and smearing corrections*: this uncertainty is implemented as migration within VBF categories, within ttH categories, within VH categories, and from tagged to untagged categories. Jet energy scale corrections account for an 8 to 18% migration between the VBF categories and 11% from the VBF to untagged categories. The migration due to the energy scale is about 5% in ttH categories and up to about 15% in VH categories. The jet energy resolution has an impact on the event migration of less than 3% in all categories except VH, for which the effect can be as large as 20%. However, the processes contributing to the VH categories and showing the largest migrations represent a marginal fraction of events, so that their effect on the results is negligible. Processes contributing to the majority of the events in the VH categories show migrations of about 3%.
- *Missing transverse energy*: this uncertainty is computed by shifting the reconstructed p_T of the particle candidates entering the computation of p_T^{miss} within the momentum scale and resolution uncertainties appropriate to each type of reconstructed object, as described in Ref. [50]. It results in a 10 to 15% migration from the ggH categories into the VH MET category.
- *Pileup jet identification*: this uncertainty is estimated by comparing in data and simulation the identification score of jets in events with a Z boson and one balanced jet. The full discrepancy between data and simulation is used to estimate the event migration, which is of the order of 1% or less.
- *Lepton isolation and identification*: for both electrons and muons the uncertainty is computed by varying the ratio of the efficiency measured in data and simulation within its uncertainty. The measurement is done using the tag-and-probe technique on Z events. The resulting differences in the selection efficiency are less than 1% for the ttH Leptonic category, 1.5% for the WH Leptonic category, and 3% for the ZH

Leptonic category.

- *b tagging efficiency*: uncertainties have been evaluated by comparing data and simulated distributions for the CSV b tagging discriminant, as described in Section 2. The uncertainties include the statistical component in the estimate of the fraction of heavy- and light-flavour jets in data and simulation, and the corresponding mutual contaminations. These are propagated differently for the hadron-tagged category and the lepton-tagged category, because the former uses the b tagging discriminant distribution as input to a specialized $t\bar{t}H$ BDT, whereas the latter uses a fixed working point, as described in Section 7. For the lepton-tagged category, the uncertainty is evaluated by varying the measured b tagging efficiencies in data and simulation within their uncertainties [22]. For the hadron-tagged category, the uncertainty is evaluated by modifying the shape of the b tagging discriminant in the simulation. The resulting uncertainty in the signal yields is about 2% in the lepton-tagged category and less than 5% in the hadron-tagged category.
- *Vertex finding efficiency*: the largest contribution to this uncertainty comes from the modelling of the underlying event, plus the uncertainty in the ratio of data and simulation obtained using $Z \rightarrow \mu^+\mu^-$ events. It is handled as an additional nuisance parameter built into the signal model, which allows the fraction of events in the correct and wrong vertex scenario to change. The size of the uncertainty in the vertex selection efficiency is 2%.
- *Integrated luminosity*: it amounts to a 2.5% uncertainty in the signal yield [51].

The choice of the background parametrization is handled using the discrete profiling method, described in Section 9, which propagates the uncertainty on the choice of function through the fits.

The dominant systematic uncertainties on the signal strengths and couplings are the photon shower shape modelling (which affects the photon identification and per-photon energy resolution estimate), the photon energy scale and smearing, the jet energy scale, the integrated luminosity. The most important theoretical uncertainties are the branching fraction, and the renormalization and factorization scale uncertainties. Each of these uncertainties has an impact of a few percent on the overall signal strength, with some dependence on the targeted production mechanism, as shown in Fig. 10.

11 Results

To extract the results, binned maximum-likelihood fits are performed to the $m_{\gamma\gamma}$ distributions of all categories, in the range $100 < m_{\gamma\gamma} < 180$ GeV, with a single overall signal strength modifier and a single value of m_H free to vary in the fit (profiled). Binned fits are used for speed of computation, and the chosen bin size of 250 MeV is sufficiently small compared to the mass resolution that no information is lost. The signal strength modifier μ is defined as the ratio of the observed Higgs boson rate in the $H \rightarrow \gamma\gamma$ decay channel to the SM expectation. The data and the signal-plus-background model fit for each category are shown in Figs. 11–13. The $m_{\gamma\gamma}$ distribution for the sum of all the categories is shown in Fig. 14. The one (green) and two (yellow) standard deviation bands shown for the background component of the fit include the uncertainty in the fitted parameters.

Table 3 and Fig. 15 show the expected number of signal events for each category. The total number is broken down by the contribution (in percent) of each production mode to any particular event category. The σ_{eff} and σ_{HM} are also listed: the former is defined as the smallest interval

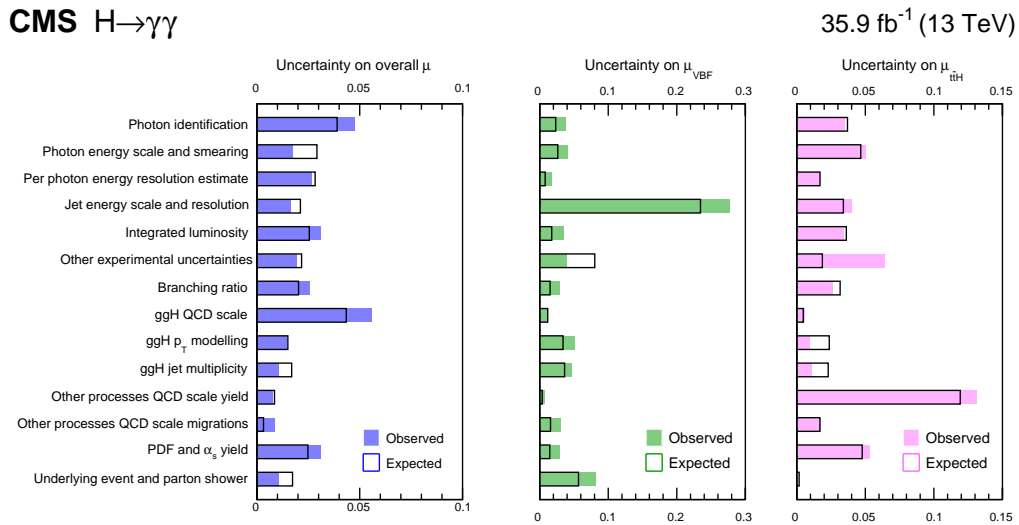


Figure 10: Summary of the impact of the different systematic uncertainties on the overall signal strength modifier and on the signal strength modifiers for the VBF and $t\bar{t}H$ production processes. The observed (expected) results are shown by the solid (empty) bars.

containing 68.3% of the invariant mass distribution, while the latter represents the width of the distribution at half of its highest point (FWHM), divided by 2.35. The table also reports the expected number of background events per GeV in the corresponding $\pm\sigma_{\text{eff}}$ window around 125 GeV, using the best fit background function.

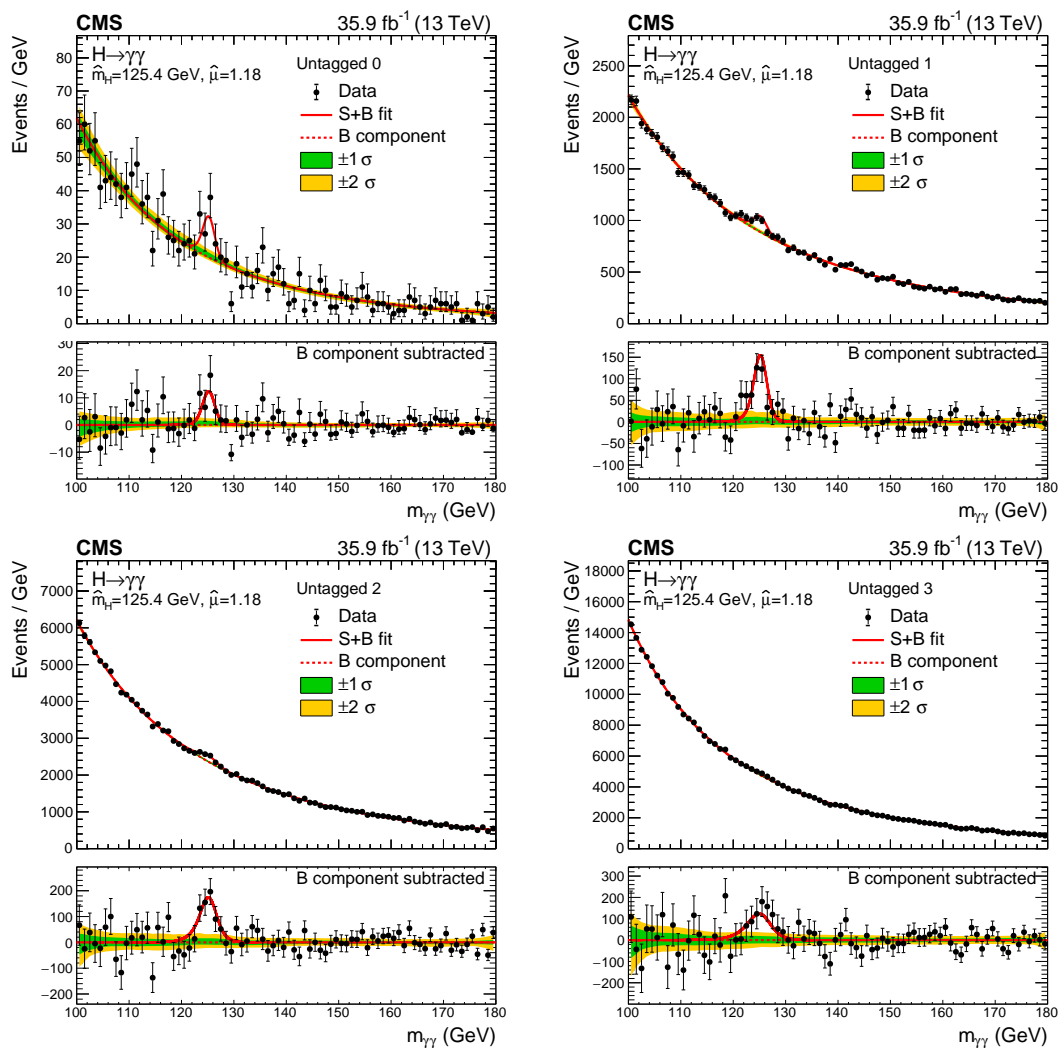


Figure 11: Data and signal-plus-background model fits in the four untagged categories are shown. The one (green) and two (yellow) standard deviation bands include the uncertainties in the background component of the fit. The lower panel in each plot shows the residuals after the background subtraction.

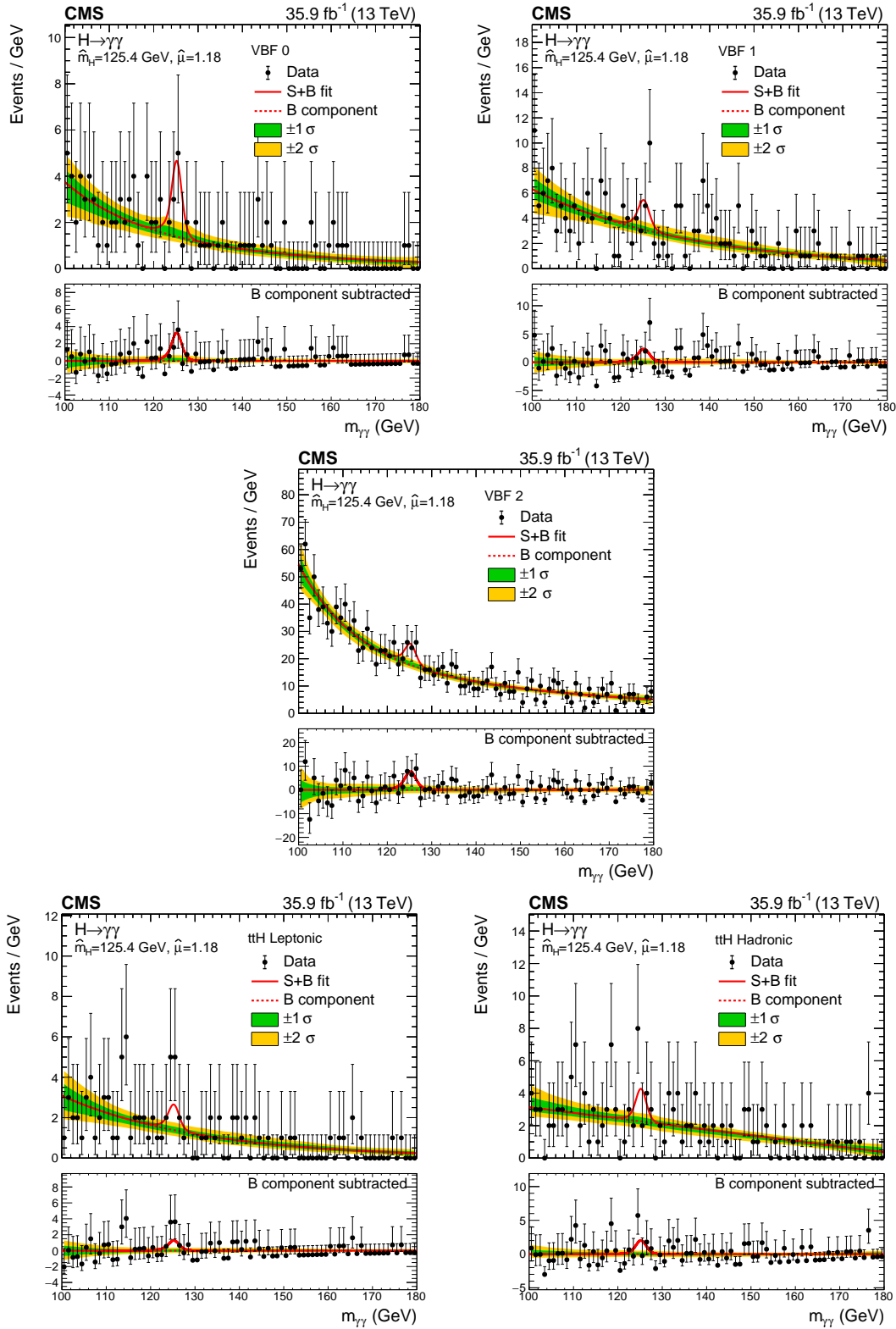


Figure 12: Data and signal-plus-background model fits in VBF and $t\bar{t}H$ categories are shown. The one (green) and two (yellow) standard deviation bands include the uncertainties in the background component of the fit. The lower panel in each plot shows the residuals after the background subtraction.

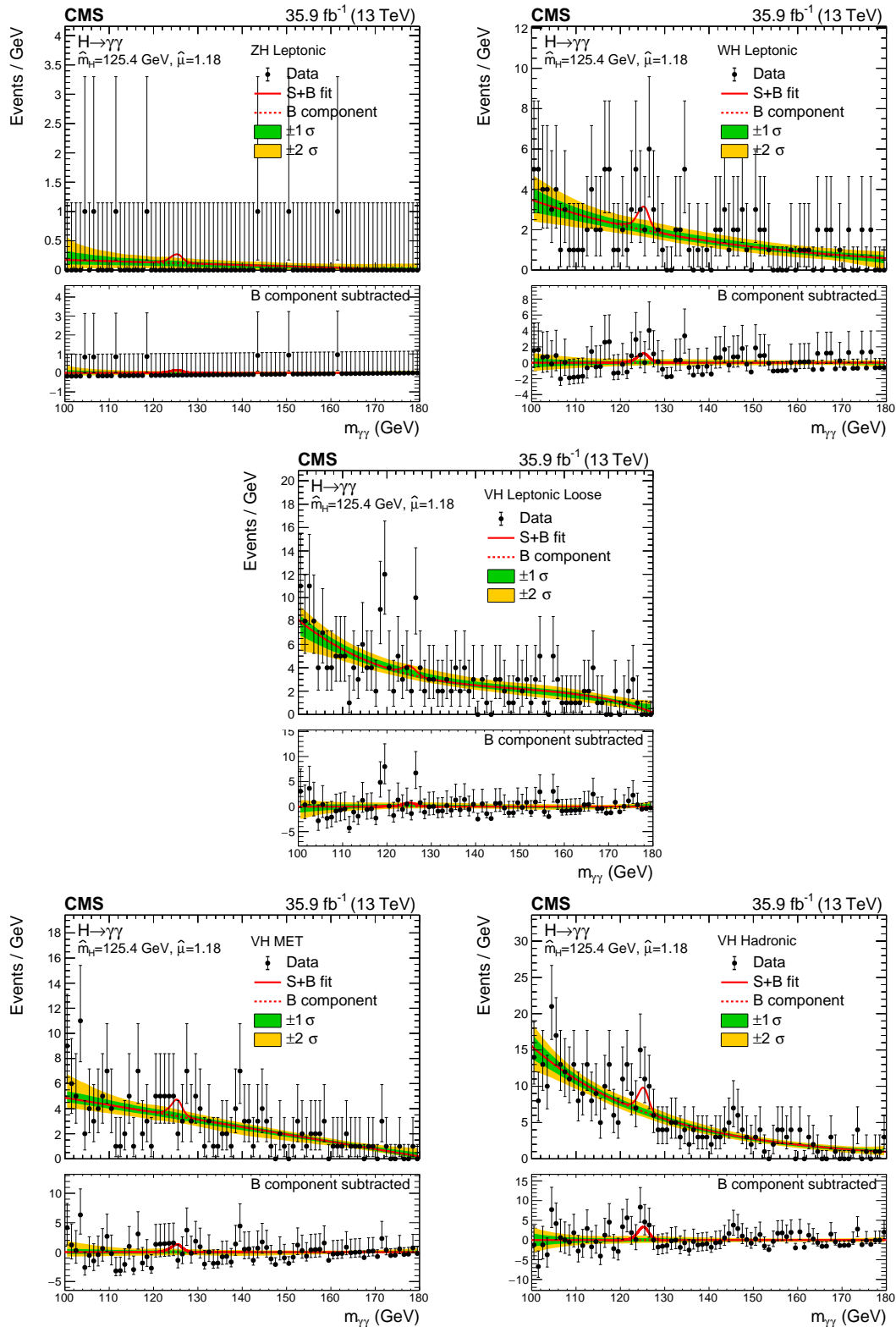


Figure 13: Data and signal-plus-background model fits in VH categories are shown. The one (green) and two (yellow) standard deviation bands include the uncertainties in the background component of the fit. The lower panel in each plot shows the residuals after the background subtraction.

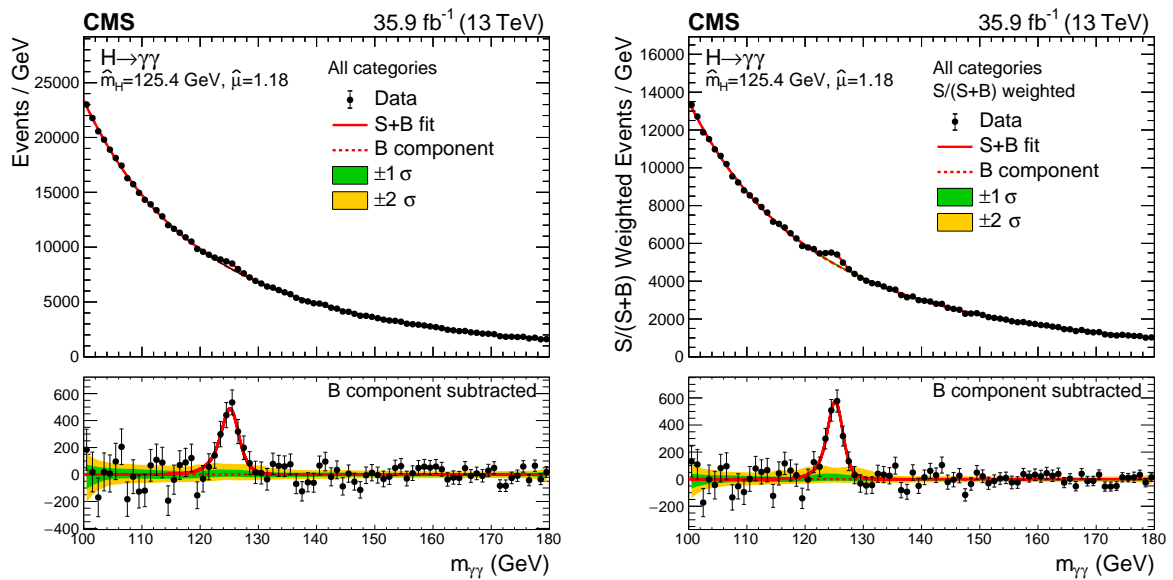


Figure 14: Data and signal-plus-background model fits for all categories summed (left) and where the categories are summed weighted by their sensitivity (right). The one (green) and two (yellow) standard deviation bands include the uncertainties in the background component of the fit. The lower panel in each plot show the residuals after the background subtraction.

Table 3: The expected number of signal events per category and the percentage breakdown per production mode in that category. The σ_{eff} , computed as the smallest interval containing 68.3% of the invariant mass distribution, and σ_{HM} , computed as the width of the distribution at half of its highest point divided by 2.35, are also shown as an estimate of the $m_{\gamma\gamma}$ resolution in that category. The expected number of background events per GeV around 125 GeV is also listed.

Event categories	Total	Expected SM 125 GeV Higgs boson signal										Bkg		
		ggH	VBF	ttH	bbH	tHq	tHW	WH lep	ZH lep	WH had	ZH had	σ_{eff} (GeV)	σ_{HM} (GeV)	(GeV^{-1})
Untagged 0	32.5	72.0 %	16.6 %	2.6 %	0.6 %	0.7 %	0.3 %	0.6 %	0.3 %	4.2 %	2.2 %	1.32	1.26	21.8
Untagged 1	469.3	86.5 %	7.9 %	0.6 %	1.2 %	0.1 %	<0.05 %	0.5 %	0.3 %	1.9 %	1.1 %	1.46	1.32	925.1
Untagged 2	678.3	89.9 %	5.4 %	0.4 %	1.2 %	0.1 %	<0.05 %	0.5 %	0.3 %	1.4 %	0.8 %	1.93	1.67	2391.7
Untagged 3	624.3	91.3 %	4.4 %	0.5 %	1.0 %	0.1 %	<0.05 %	0.5 %	0.3 %	1.2 %	0.7 %	2.61	2.27	4855.1
VBF 0	9.3	15.5 %	83.2 %	0.4 %	0.4 %	0.3 %	<0.05 %	<0.05 %	<0.05 %	0.2 %	<0.05 %	1.52	1.31	1.6
VBF 1	8.0	28.4 %	69.7 %	0.4 %	0.6 %	0.4 %	<0.05 %	0.1 %	<0.05 %	0.3 %	0.1 %	1.66	1.38	3.3
VBF 2	25.2	45.1 %	51.2 %	0.9 %	0.8 %	0.6 %	0.1 %	0.2 %	0.1 %	0.8 %	0.3 %	1.64	1.37	18.9
ttH Hadronic	5.6	7.0 %	0.7 %	81.1 %	2.1 %	4.3 %	2.1 %	0.1 %	0.1 %	0.7 %	1.9 %	1.48	1.30	2.4
ttH Leptonic	3.8	1.5 %	<0.05 %	87.8 %	0.1 %	4.7 %	3.1 %	1.5 %	1.2 %	<0.05 %	<0.05 %	1.60	1.35	1.5
ZH Leptonic	0.5	<0.05 %	<0.05 %	2.6 %	<0.05 %	<0.05 %	0.1 %	<0.05 %	97.3 %	<0.05 %	<0.05 %	1.65	1.43	0.1
WH Leptonic	3.6	1.3 %	0.6 %	5.2 %	0.2 %	3.0 %	0.7 %	84.5 %	4.3 %	0.1 %	0.1 %	1.64	1.43	2.1
VH LeptonicLoose	2.7	8.1 %	2.7 %	2.4 %	0.6 %	1.8 %	0.1 %	64.4 %	19.1 %	0.6 %	0.2 %	1.67	1.56	3.5
VH Hadronic	7.9	47.6 %	4.5 %	4.4 %	0.4 %	1.7 %	0.3 %	0.2 %	0.5 %	25.2 %	15.1 %	1.38	1.30	7.2
VH MET	4.0	18.7 %	2.6 %	15.4 %	0.4 %	2.1 %	1.2 %	26.8 %	30.4 %	1.4 %	0.9 %	1.56	1.39	3.5
Total	1875.0	86.9 %	7.1 %	1.0 %	1.1 %	0.2 %	<0.05 %	0.8 %	0.4 %	1.6 %	0.9 %	1.96	1.62	8237.8

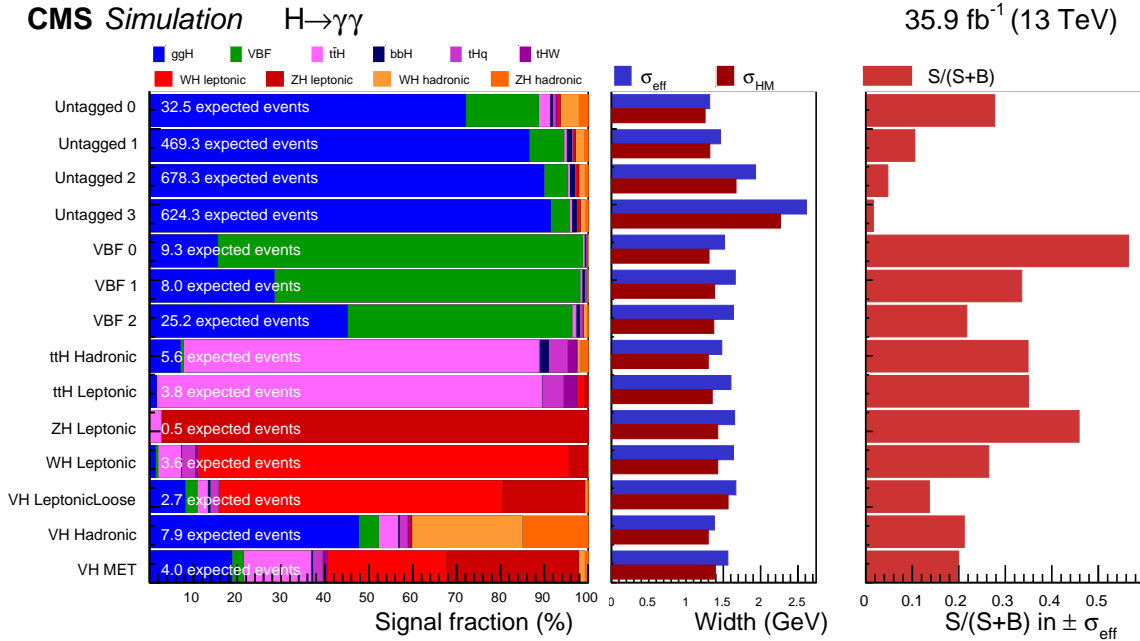


Figure 15: Expected fraction of signal events per production mode in the different categories. For each category, the σ_{eff} and σ_{HM} of the signal model, as described in the text, are given. The ratio of the number of signal events (S) to the number of signal-plus-background events (S+B) is shown on the right hand side.

A likelihood scan of the signal strength modifier is performed, with other parameters of the signal and background models allowed to vary. Systematic uncertainties are included in the form of nuisance parameters and the results are obtained using an asymptotic approach [52–54] with a test statistic based on the profile likelihood ratio (q) [55]. The individual contributions of the statistical and systematic uncertainties are separated by performing a likelihood scan removing the systematic uncertainties to determine the statistical uncertainty. The systematic uncertainty is then taken as the difference in quadrature between the total uncertainty and the statistical uncertainty. The results can be found in Fig. 16. The best fit signal strength modifier measured for all categories combined using this method is $\hat{\mu} = 1.18^{+0.17}_{-0.14} = 1.18^{+0.12}_{-0.11}(\text{stat})^{+0.09}_{-0.07}(\text{syst})^{+0.07}_{-0.06}(\text{theo})$. The best fit mass is found at $\hat{m}_H = 125.4 \pm 0.3 \text{ GeV} = 125.4 \pm 0.2(\text{stat}) \pm 0.2(\text{syst}) \text{ GeV}$, compatible with the combined mass measurement from ATLAS and CMS [7]. A precise determination of the systematic uncertainties affecting the best fit mass is not within the scope of this analysis. The maximum relative variation of $\hat{\mu}$ for m_H within a range of $\pm 1 \text{ GeV}$ around 125 GeV is less than 2%.

The results of a fit to the signal strength modifier for each production mode, defined analogously to the overall μ above, are shown in Fig. 17 and summarized in Table 4. The observed rates of the VBF, $t\bar{t}H$, and VH production modes correspond respectively to p -values of 4.2, 0.074, and 0.47%, with respect to the absence of the considered production mode. The expected p -values are 1.8, 7.3, and 12%, respectively, for an SM Higgs boson, with the current data set.

A similar fit is performed to extract the ratios of observed cross sections to the SM prediction in the stage 0 of the simplified template cross section (STXS) framework [32]. These cross sections are for a reduced fiducial volume, defined by requiring the Higgs boson rapidity to be less than 2.5. Outside of this volume the analysis has a negligible acceptance. The ratios are measured for the ggH, VBF, $t\bar{t}H$, and VH production processes. VH is further split considering the decay of the associated boson into WH leptonic, ZH leptonic, and VH hadronic, which groups hadronic

Table 4: Results of the fit to the signal strength modifier for each production mode. The total uncertainties as well as their statistical, systematic, and theory components are shown. The last two columns report the p -value relative to the observed rates and referred to the absence of the considered production mode, and its corresponding estimated significance.

Process	$\hat{\mu}$	Uncertainties				p -value	Estimated significance (standard deviations)
		tot	stat	syst	theo		
ggH	1.10	+0.20 -0.18	+0.15 -0.15	+0.09 -0.08	+0.08 -0.06	3.1×10^{-12}	6.9
VBF	0.8	+0.6 -0.5	+0.5 -0.4	+0.3 -0.2	+0.2 -0.1	4.2×10^{-2}	1.7
$t\bar{t}H$	2.2	+0.9 -0.8	+0.9 -0.8	+0.2 -0.1	+0.2 -0.1	7.4×10^{-4}	3.2
VH	2.4	+1.1 -1.0	+1.0 -1.0	+0.2 -0.1	+0.2 -0.1	4.7×10^{-3}	2.6

decays of both the W and Z bosons. The STXS approach differs from the signal strength modifier measurements in the splitting of the production modes, and reduces the dependence of the measurements on the theoretical uncertainties in the SM predictions, by avoiding the sizeable uncertainty associated with the extrapolation to the full phase space. The measured cross section ratios, where the SM prediction [32] is denoted as σ_{theo} , are shown in Fig. 18.

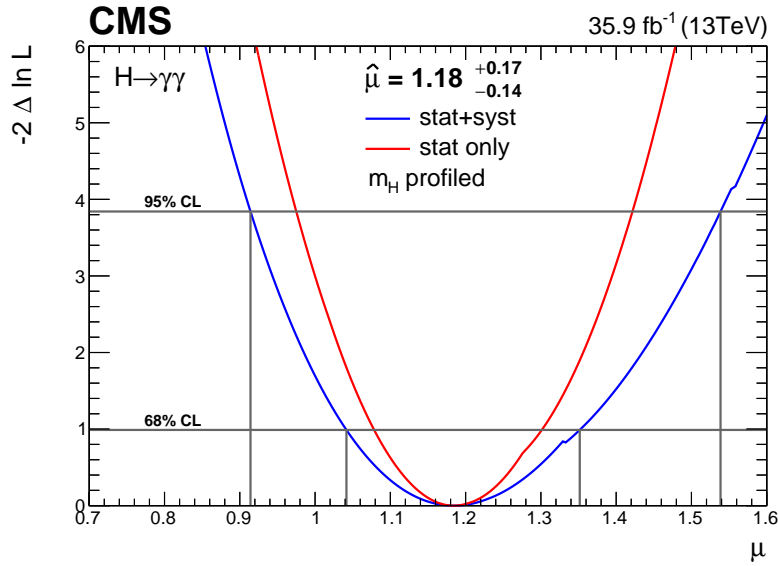


Figure 16: The likelihood scan for the signal strength modifier where the value of the SM Higgs boson mass is profiled in the fit.

A two-dimensional likelihood scan of the signal strength modifier $\mu_{\text{ggH}, t\bar{t}H}$ for fermionic production modes (ggH and $t\bar{t}H$) and $\mu_{\text{VBF}, \text{VH}}$ for vector boson production modes (VBF, ZH, WH), with the value of the parameter m_H profiled in the fit, is performed. Figure 19 shows the 68 and 95% confidence level (CL) contours. The best fit values for each modifier are $\hat{\mu}_{\text{ggH}, t\bar{t}H} = 1.19^{+0.22}_{-0.18}$ and $\hat{\mu}_{\text{VBF}, \text{VH}} = 1.21^{+0.58}_{-0.51}$.

Deviations from the SM expectation in the couplings of the Higgs boson can be parameterized using coupling modifiers in the so-called κ framework [17]. Two-dimensional likelihood scans of the Higgs boson coupling modifiers are produced: κ_f versus κ_V , the coupling modifiers to fermions and bosons; and κ_g versus κ_γ , the effective coupling modifiers to gluons and photons. The κ parameters other than those varied are fixed to 1 in each case. Figure 20 shows the test statistic q and the 68% and 95% CL contours for each scan. The point $(\kappa_V, \kappa_f) = (1, -1)$ has an observed (expected) q value of 35.2 (53.7), inconsistent with the observed (expected) best fit

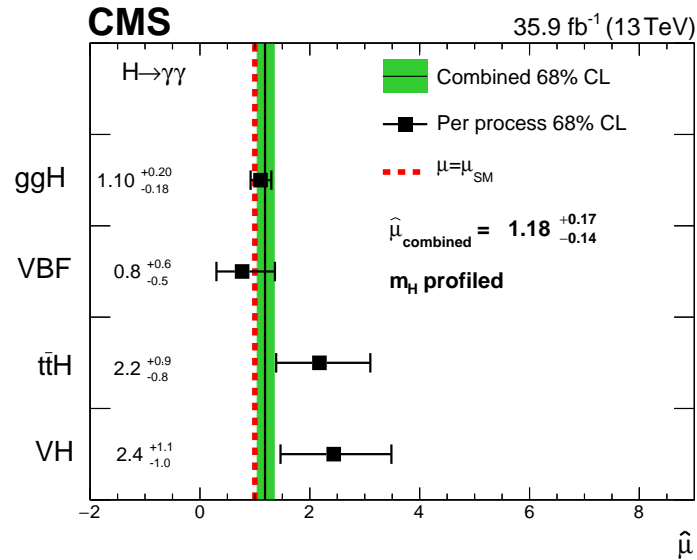


Figure 17: Signal strength modifiers measured for each process (black points), with the SM Higgs boson mass profiled, compared to the overall signal strength modifier (green band) and to the SM expectation (dashed red line).

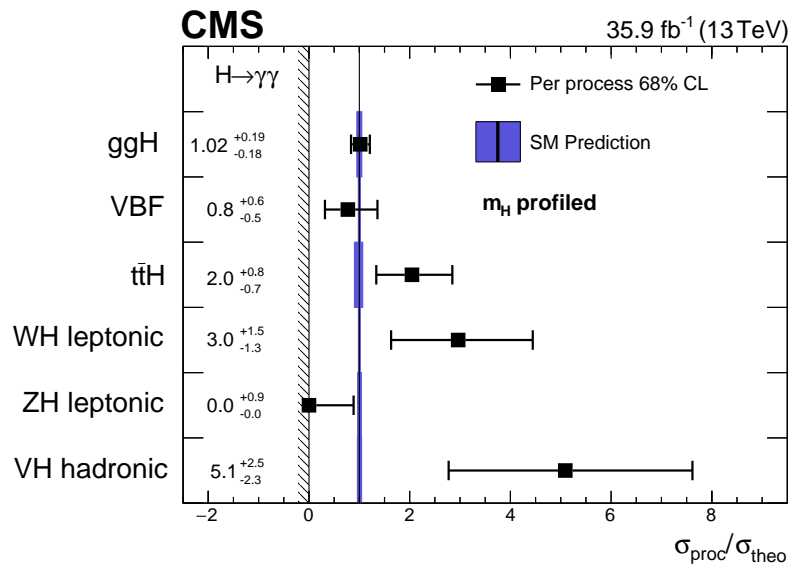


Figure 18: Cross section ratios measured for each process (black points) in the Higgs simplified template cross section framework [32], with the SM Higgs boson mass profiled, compared to the SM expectations and their uncertainties (blue band). The signal strength modifiers are constrained to be nonnegative, as indicated by the vertical line and hashed pattern at zero.

value at the level of 5.8 (7.0) standard deviations.

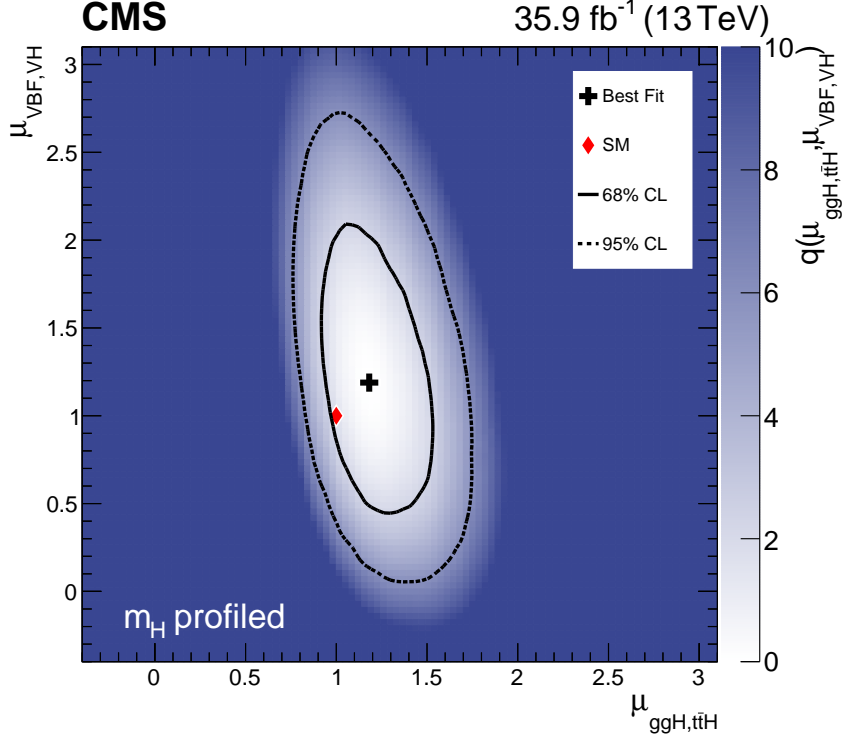


Figure 19: The two-dimensional best fit (black cross) of the signal strength modifiers for fermionic (ggH, t̄tH) and bosonic (VBF, ZH, WH) production modes compared to the SM expectation (red diamond). The Higgs boson mass is profiled in the fit. The solid (dashed) line represents the 68 (95)% confidence region.

12 Summary

We report measurements of the production cross section and couplings of the Higgs boson using its diphoton decay: the overall signal strength modifier; the signal strength modifier for each production mode separately; cross section ratios for the stage 0 simplified template cross section framework; the best fit rates in the $\mu_{\text{VBF,VH}}-\mu_{\text{ggH,t̄tH}}$ plane with VBF and VH production, and ggH and t̄tH production, varied together; and the best fit coupling modifiers in the $\kappa_f-\kappa_V$ and $\kappa_g-\kappa_\gamma$ planes. The analysis is based on proton-proton collision data collected at $\sqrt{s} = 13$ TeV by the CMS experiment at the LHC in 2016, corresponding to an integrated luminosity of 35.9 fb^{-1} . The best fit signal strength modifier obtained after profiling m_H is $\hat{\mu} = 1.18^{+0.17}_{-0.14} = 1.18^{+0.12}_{-0.11} (\text{stat})^{+0.09}_{-0.07} (\text{syst})^{+0.07}_{-0.06} (\text{theo})$. The best fit values in the $\mu_{\text{VBF,VH}}-\mu_{\text{ggH,t̄tH}}$ plane are $\hat{\mu}_{\text{ggH,t̄tH}} = 1.19^{+0.22}_{-0.18}$ and $\hat{\mu}_{\text{VBF,VH}} = 1.21^{+0.58}_{-0.51}$. When $\mu_{\text{t̄tH}}$ is considered separately, the best fit value is $\hat{\mu}_{\text{t̄tH}} = 2.2^{+0.9}_{-0.8}$, corresponding to a p -value of 0.074% with respect to the absence of t̄tH production. Stage 0 simplified template cross sections are compatible with the standard model.

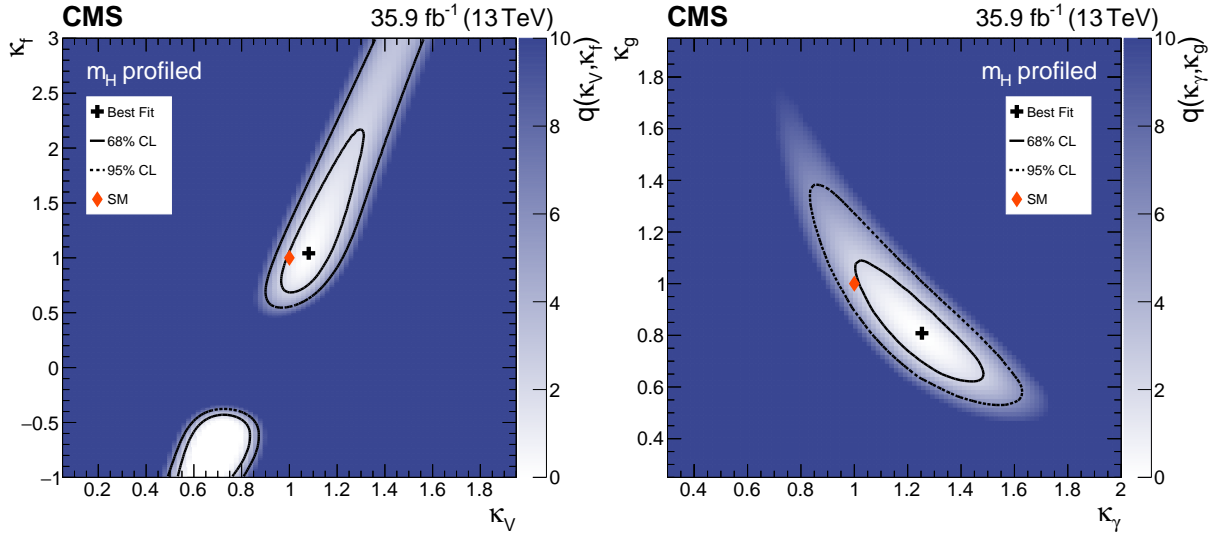


Figure 20: Two-dimensional likelihood scans of κ_f versus κ_V (left) and κ_g versus κ_γ (right). All four variables are expressed relative to the SM expectations. The mass of the Higgs boson is profiled in the fits. The crosses indicate the best fit values, the diamonds indicate the standard model expectations. The colour maps indicate the value of the test statistic q as described in the text.

Acknowledgments

We congratulate our colleagues in the CERN accelerator departments for the excellent performance of the LHC and thank the technical and administrative staffs at CERN and at other CMS institutes for their contributions to the success of the CMS effort. In addition, we gratefully acknowledge the computing centres and personnel of the Worldwide LHC Computing Grid for delivering so effectively the computing infrastructure essential to our analyses. Finally, we acknowledge the enduring support for the construction and operation of the LHC and the CMS detector provided by the following funding agencies: the Austrian Federal Ministry of Science, Research and Economy and the Austrian Science Fund; the Belgian Fonds de la Recherche Scientifique, and Fonds voor Wetenschappelijk Onderzoek; the Brazilian Funding Agencies (CNPq, CAPES, FAPERJ, and FAPESP); the Bulgarian Ministry of Education and Science; CERN; the Chinese Academy of Sciences, Ministry of Science and Technology, and National Natural Science Foundation of China; the Colombian Funding Agency (COLCIENCIAS); the Croatian Ministry of Science, Education and Sport, and the Croatian Science Foundation; the Research Promotion Foundation, Cyprus; the Secretariat for Higher Education, Science, Technology and Innovation, Ecuador; the Ministry of Education and Research, Estonian Research Council via IUT23-4 and IUT23-6 and European Regional Development Fund, Estonia; the Academy of Finland, Finnish Ministry of Education and Culture, and Helsinki Institute of Physics; the Institut National de Physique Nucléaire et de Physique des Particules / CNRS, and Commissariat à l'Énergie Atomique et aux Énergies Alternatives / CEA, France; the Bundesministerium für Bildung und Forschung, Deutsche Forschungsgemeinschaft, and Helmholtz-Gemeinschaft Deutscher Forschungszentren, Germany; the General Secretariat for Research and Technology, Greece; the National Research, Development and Innovation Fund, Hungary; the Department of Atomic Energy and the Department of Science and Technology, India; the Institute for Studies in Theoretical Physics and Mathematics, Iran; the Science Foundation, Ireland; the Istituto Nazionale di Fisica Nucleare, Italy; the Ministry of Science, ICT and Fu-

ture Planning, and National Research Foundation (NRF), Republic of Korea; the Lithuanian Academy of Sciences; the Ministry of Education, and University of Malaya (Malaysia); the Mexican Funding Agencies (BUAP, CINVESTAV, CONACYT, LNS, SEP, and UASLP-FAI); the Ministry of Business, Innovation and Employment, New Zealand; the Pakistan Atomic Energy Commission; the Ministry of Science and Higher Education and the National Science Centre, Poland; the Fundação para a Ciência e a Tecnologia, Portugal; JINR, Dubna; the Ministry of Education and Science of the Russian Federation, the Federal Agency of Atomic Energy of the Russian Federation, Russian Academy of Sciences and the Russian Foundation for Basic Research; the Ministry of Education, Science and Technological Development of Serbia; the Secretaría de Estado de Investigación, Desarrollo e Innovación, Programa Consolider-Ingenio 2010, Plan Estatal de Investigación Científica y Técnica y de Innovación 2013-2016, Plan de Ciencia, Tecnología e Innovación 2013-2017 del Principado de Asturias and Fondo Europeo de Desarrollo Regional, Spain; the Swiss Funding Agencies (ETH Board, ETH Zurich, PSI, SNF, UniZH, Canton Zurich, and SER); the Ministry of Science and Technology, Taipei; the Thailand Center of Excellence in Physics, the Institute for the Promotion of Teaching Science and Technology of Thailand, Special Task Force for Activating Research and the National Science and Technology Development Agency of Thailand; the Scientific and Technical Research Council of Turkey, and Turkish Atomic Energy Authority; the National Academy of Sciences of Ukraine, and State Fund for Fundamental Researches, Ukraine; the Science and Technology Facilities Council, UK; the US Department of Energy, and the US National Science Foundation.

Individuals have received support from the Marie-Curie programme and the European Research Council and Horizon 2020 Grant, contract No. 675440 (European Union); the Leventis Foundation; the A. P. Sloan Foundation; the Alexander von Humboldt Foundation; the Belgian Federal Science Policy Office; the Fonds pour la Formation à la Recherche dans l'Industrie et dans l'Agriculture (FRIA-Belgium); the Agentschap voor Innovatie door Wetenschap en Technologie (IWT-Belgium); the F.R.S.-FNRS and FWO (Belgium) under the "Excellence of Science - EOS" - be.h project n. 30820817; the Ministry of Education, Youth and Sports (MEYS) of the Czech Republic; the Lendület ("Momentum") Programme and the János Bolyai Research Scholarship of the Hungarian Academy of Sciences, the New National Excellence Program ÚNKP, the NKFI research grants 123842, 123959, 124845, 124850 and 125105 (Hungary); the Council of Scientific and Industrial Research, India; the HOMING PLUS programme of the Foundation for Polish Science, cofinanced from European Union, Regional Development Fund, the Mobility Plus programme of the Ministry of Science and Higher Education, the National Science Center (Poland), contracts Harmonia 2014/14/M/ST2/00428, Opus 2014/13/B/ST2/02543, 2014/15/B/ST2/03998, and 2015/19/B/ST2/02861, Sonata-bis 2012/07/E/ST2/01406; the National Priorities Research Program by Qatar National Research Fund; the Programa de Excelencia María de Maeztu and the Programa Severo Ochoa del Principado de Asturias; the Thalís and Aristeia programmes cofinanced by EU-ESF and the Greek NSRF; the Rachadapisek Sompot Fund for Postdoctoral Fellowship, Chulalongkorn University and the Chulalongkorn Academic into Its 2nd Century Project Advancement Project (Thailand); the Welch Foundation, contract C-1845; and the Weston Havens Foundation (USA).

References

- [1] S. L. Glashow, "Partial-symmetries of weak interactions", *Nucl. Phys.* **22** (1961) 579, doi:10.1016/0029-5582(61)90469-2.
- [2] S. Weinberg, "A model of leptons", *Phys. Rev. Lett.* **19** (1967) 1264, doi:10.1103/PhysRevLett.19.1264.

- [3] A. Salam, "Weak and electromagnetic interactions", in *Elementary particle physics: relativistic groups and analyticity*, N. Svartholm, ed., p. 367. Almqvist & Wiskell, 1968. Proceedings of the eighth Nobel symposium.
- [4] ATLAS Collaboration, "Observation of a new particle in the search for the standard model Higgs boson with the ATLAS detector at the LHC", *Phys. Lett. B* **716** (2012) 1, doi:10.1016/j.physletb.2012.08.020, arXiv:1207.7214.
- [5] CMS Collaboration, "Observation of a new boson at a mass of 125 GeV with the CMS experiment at the LHC", *Phys. Lett. B* **716** (2012) 30, doi:10.1016/j.physletb.2012.08.021, arXiv:1207.7235.
- [6] CMS Collaboration, "Observation of a new boson with mass near 125 GeV in pp collisions at $\sqrt{s} = 7$ and 8 TeV", *JHEP* **06** (2013) 081, doi:10.1007/JHEP06(2013)081, arXiv:1303.4571.
- [7] ATLAS and CMS Collaborations, "Combined measurement of the Higgs boson mass in pp collisions at $\sqrt{s} = 7$ and 8 TeV with the ATLAS and CMS experiments", *Phys. Rev. Lett.* **114** (2015) 191803, doi:10.1103/PhysRevLett.114.191803, arXiv:1503.07589.
- [8] ATLAS and CMS Collaborations, "Measurements of the Higgs boson production and decay rates and constraints on its couplings from a combined ATLAS and CMS analysis of the LHC pp collision data at $\sqrt{s} = 7$ and 8 TeV", *JHEP* **08** (2016) 045, doi:10.1007/JHEP08(2016)045, arXiv:1606.02266.
- [9] F. Englert and R. Brout, "Broken symmetry and the mass of gauge vector mesons", *Phys. Rev. Lett.* **13** (1964) 321, doi:10.1103/PhysRevLett.13.321.
- [10] P. W. Higgs, "Broken symmetries, massless particles and gauge fields", *Phys. Lett.* **12** (1964) 132, doi:10.1016/0031-9163(64)91136-9.
- [11] P. W. Higgs, "Broken symmetries and the masses of gauge bosons", *Phys. Rev. Lett.* **13** (1964) 508, doi:10.1103/PhysRevLett.13.508.
- [12] G. S. Guralnik, C. R. Hagen, and T. W. B. Kibble, "Global conservation laws and massless particles", *Phys. Rev. Lett.* **13** (1964) 585, doi:10.1103/PhysRevLett.13.585.
- [13] P. W. Higgs, "Spontaneous symmetry breakdown without massless bosons", *Phys. Rev.* **145** (1966) 1156, doi:10.1103/PhysRev.145.1156.
- [14] T. W. B. Kibble, "Symmetry breaking in non-Abelian gauge theories", *Phys. Rev.* **155** (1967) 1554, doi:10.1103/PhysRev.155.1554.
- [15] CMS Collaboration, "Observation of the diphoton decay of the Higgs boson and measurement of its properties", *Eur. Phys. J. C* **74** (2014) 3076, doi:10.1140/epjc/s10052-014-3076-z, arXiv:1407.0558.
- [16] ATLAS Collaboration, "Measurement of Higgs boson production in the diphoton decay channel in pp collisions at center-of-mass energies of 7 and 8 TeV with the ATLAS detector", *Phys. Rev. D* **90** (2014) 112015, doi:10.1103/PhysRevD.90.112015, arXiv:1408.7084.

-
- [17] LHC Higgs Cross Section Working Group, “Handbook of LHC Higgs Cross Sections: 3. Higgs Properties”, Technical Report CERN-2013-004, CERN, 2013.
doi:10.5170/CERN-2013-004, arXiv:1307.1347.
- [18] CMS Collaboration, “Energy calibration and resolution of the CMS electromagnetic calorimeter in pp collisions at $\sqrt{s} = 7$ TeV”, *JINST* **8** (2013) P09009,
doi:10.1088/1748-0221/8/09/P09009, arXiv:1306.2016.
- [19] CMS Collaboration, “Particle-flow reconstruction and global event description with the CMS detector”, *JINST* **12** (2017) P10003, doi:10.1088/1748-0221/12/10/P10003,
arXiv:1706.04965.
- [20] M. Cacciari, G. P. Salam, and G. Soyez, “The anti- k_T jet clustering algorithm”, *JHEP* **04** (2008) 063, doi:10.1088/1126-6708/2008/04/063, arXiv:0802.1189.
- [21] CMS Collaboration, “Jet energy scale and resolution in the CMS experiment in pp collisions at 8 TeV”, *JINST* **12** (2017) P02014,
doi:10.1088/1748-0221/12/02/P02014, arXiv:1607.03663.
- [22] CMS Collaboration, “Identification of b-quark jets with the CMS experiment”, *JINST* **8** (2013) P04013, doi:10.1088/1748-0221/8/04/P04013, arXiv:1211.4462.
- [23] CMS Collaboration, “Identification of heavy-flavour jets with the CMS detector in pp collisions at 13 TeV”, (2017). arXiv:1712.07158. Submitted to JINST.
- [24] CMS Collaboration, “The CMS experiment at the CERN LHC”, *JINST* **3** (2008) S08004,
doi:10.1088/1748-0221/3/08/S08004.
- [25] CMS Collaboration, “Measurement of the inclusive W and Z production cross sections in pp collisions at $\sqrt{s} = 7$ TeV with the CMS experiment”, *JHEP* **10** (2011) 132,
doi:10.1007/JHEP10(2011)132, arXiv:1107.4789.
- [26] J. Alwall et al., “The automated computation of tree-level and next-to-leading order differential cross sections, and their matching to parton shower simulations”, *JHEP* **07** (2014) 079, doi:10.1007/JHEP07(2014)079, arXiv:1405.0301.
- [27] R. Frederix and S. Frixione, “Merging meets matching in MC@NLO”, *JHEP* **12** (2012) 061, doi:10.1007/JHEP12(2012)061, arXiv:1209.6215.
- [28] T. Sjöstrand, S. Mrenna, and P. Z. Skands, “A brief introduction to PYTHIA 8.1”, *Comput. Phys. Commun.* **178** (2008) 852, doi:10.1016/j.cpc.2008.01.036,
arXiv:0710.3820.
- [29] CMS Collaboration, “Event generator tunes obtained from underlying event and multiparton scattering measurements”, *Eur. Phys. J. C* **76** (2016) 155,
doi:10.1140/epjc/s10052-016-3988-x, arXiv:1512.00815.
- [30] K. Hamilton, P. Nason, E. Re, and G. Zanderighi, “NNLOPS simulation of Higgs boson production”, *JHEP* **10** (2013) 222, doi:10.1007/JHEP10(2013)222,
arXiv:1309.0017.
- [31] NNPDF Collaboration, “Parton distributions for the LHC Run II”, *JHEP* **04** (2015) 040,
doi:10.1007/JHEP04(2015)040, arXiv:1410.8849.

- [32] LHC Higgs Cross Section Working Group, “Handbook of LHC Higgs cross sections: 4. Deciphering the nature of the Higgs sector”, Technical Report CERN-2017-002-M, CERN, 2017. doi:10.23731/CYRM-2017-002, arXiv:1610.07922.
- [33] T. Gleisberg, S. Hoeche, F. Krauss, M. Schonherr, S. Schumann, F. Siegert, and J. Winter, “Event generation with SHERPA 1.1”, *JHEP* **02** (2009) 007, doi:10.1088/1126-6708/2009/02/007, arXiv:0811.4622.
- [34] GEANT4 Collaboration, “GEANT4—a simulation toolkit”, *Nucl. Instrum. Meth. A* **506** (2003) 250, doi:10.1016/S0168-9002(03)01368-8.
- [35] CMS Collaboration, “Performance of photon reconstruction and identification with the CMS detector in proton-proton collisions at $\sqrt{s} = 8$ TeV”, *JINST* **10** (2015) P08010, doi:10.1088/1748-0221/10/08/P08010, arXiv:1502.02702.
- [36] M. Cacciari, G. P. Salam, and G. Soyez, “FastJet user manual”, *Eur. Phys. J. C* **72** (2012) 1896, doi:10.1140/epjc/s10052-012-1896-2, arXiv:1111.6097.
- [37] CMS Collaboration, “Electron and photon performance using data collected by CMS at $\sqrt{s} = 13$ TeV and 25 ns”, CMS Detector Performance Report CMS-DP-2015-067, 2015.
- [38] P. D. Dauncey, M. Kenzie, N. Wardle, and G. J. Davies, “Handling uncertainties in background shapes: the discrete profiling method”, *JINST* **10** (2015) P04015, doi:10.1088/1748-0221/10/04/P04015, arXiv:1408.6865.
- [39] R. A. Fisher, “On the Interpretation of χ^2 from Contingency Tables, and the Calculation of p ”, *J. Royal Stat. Soc* **85** (1922) 87, doi:10.2307/2340521.
- [40] J. Butterworth et al., “PDF4LHC recommendations for LHC Run II”, *J. Phys. G* **43** (2016) 023001, doi:10.1088/0954-3899/43/2/023001, arXiv:1510.03865.
- [41] S. Carrazza et al., “An unbiased Hessian representation for Monte Carlo PDFs”, *Eur. Phys. J. C* **75** (2015) 369, doi:10.1140/epjc/s10052-015-3590-7, arXiv:1505.06736.
- [42] CMS Collaboration, “Measurements of $t\bar{t}$ cross sections in association with b jets and inclusive jets and their ratio using dilepton final states in pp collisions at $\sqrt{s} = 13$ TeV”, *Phys. Lett. B* **776** (2018) 355, doi:10.1016/j.physletb.2017.11.043, arXiv:1705.10141.
- [43] I. W. Stewart, F. J. Tackmann, J. R. Walsh, and S. Zuberi, “Jet p_t resummation in Higgs production at NNLL’ + NNLO”, *Phys. Rev. D* **89** (2014) 054001, doi:10.1103/PhysRevD.89.054001, arXiv:1307.1808.
- [44] X. Liu and F. Petriello, “Reducing theoretical uncertainties for exclusive Higgs-boson plus one-jet production at the LHC”, *Phys. Rev. D* **87** (2013) 094027, doi:10.1103/PhysRevD.87.094027, arXiv:1303.4405.
- [45] R. Boughezal, X. Liu, F. Petriello, F. J. Tackmann, and J. R. Walsh, “Combining resummed Higgs predictions across jet bins”, *Phys. Rev. D* **89** (2014) 074044, doi:10.1103/PhysRevD.89.074044, arXiv:1312.4535.
- [46] J. M. Campbell and R. K. Ellis, “MCFM for the Tevatron and the LHC”, *Nucl. Phys. Proc. Suppl.* **205-206** (2010) 10, doi:10.1016/j.nuclphysbps.2010.08.011, arXiv:1007.3492.

- [47] I. W. Stewart and F. J. Tackmann, "Theory uncertainties for Higgs and other searches using jet bins", *Phys. Rev. D* **85** (2012) 034011, doi:10.1103/PhysRevD.85.034011, arXiv:1107.2117.
- [48] S. Gangal and F. J. Tackmann, "Next-to-leading-order uncertainties in Higgs+2 jets from gluon fusion", *Phys. Rev. D* **87** (2013) 093008, doi:10.1103/PhysRevD.87.093008, arXiv:1302.5437.
- [49] S. M. Seltzer and M. J. Berger, "Transmission and reflection of electrons by foils", *Nucl. Instrum. Meth.* **119** (1974) 157, doi:10.1016/0029-554X(74)90747-2.
- [50] CMS Collaboration, "Performance of missing energy reconstruction in 13 TeV pp collision data using the CMS detector", CMS Physics Analysis Summary CMS-PAS-JME-16-004, 2016.
- [51] CMS Collaboration, "CMS luminosity measurements for the 2016 data taking period", CMS Physics Analysis Summary CMS-PAS-LUM-17-001, 2017.
- [52] ATLAS and CMS Collaborations, LHC Higgs Combination Group, "Procedure for the LHC Higgs boson search combination in summer 2011", CMS/ATLAS joint note ATL-PHYS-PUB-2011-11, CMS NOTE 2011/005, 2011.
- [53] T. Junk, "Confidence level computation for combining searches with small statistics", *Nucl. Instrum. Meth. A* **434** (1999) 435, doi:10.1016/S0168-9002(99)00498-2, arXiv:hep-ex/9902006.
- [54] A. L. Read, "Presentation of search results: The cl_s technique", *J. Phys. G* **28** (2002) 2693, doi:10.1088/0954-3899/28/10/313.
- [55] G. Cowan, K. Cranmer, E. Gross, and O. Vitells, "Asymptotic formulae for likelihood-based tests of new physics", *Eur. Phys. J. C* **71** (2011) 1, doi:10.1140/epjc/s10052-011-1554-0, arXiv:1007.1727. [Erratum: doi:10.1140/epjc/s10052-013-2501-z].

A The CMS Collaboration

Yerevan Physics Institute, Yerevan, Armenia

A.M. Sirunyan, A. Tumasyan

Institut für Hochenergiephysik, Wien, Austria

W. Adam, F. Ambrogio, E. Asilar, T. Bergauer, J. Brandstetter, E. Brondolin, M. Dragicevic, J. Erö, A. Escalante Del Valle, M. Flechl, M. Friedl, R. Frühwirth¹, V.M. Ghete, J. Grossmann, J. Hrubec, M. Jeitler¹, A. König, N. Krammer, I. Krätschmer, D. Liko, T. Madlener, I. Mikulec, E. Pree, N. Rad, H. Rohringer, J. Schieck¹, R. Schöfbeck, M. Spanring, D. Spitzbart, A. Taurok, W. Waltenberger, J. Wittmann, C.-E. Wulz¹, M. Zarucki

Institute for Nuclear Problems, Minsk, Belarus

V. Chekhovsky, V. Mossolov, J. Suarez Gonzalez

Universiteit Antwerpen, Antwerpen, Belgium

E.A. De Wolf, D. Di Croce, X. Janssen, J. Lauwers, M. Pieters, M. Van De Klundert, H. Van Haevermaet, P. Van Mechelen, N. Van Remortel

Vrije Universiteit Brussel, Brussel, Belgium

S. Abu Zeid, F. Blekman, J. D'Hondt, I. De Bruyn, J. De Clercq, K. Deroover, G. Flouris, D. Lontkovskyi, S. Lowette, I. Marchesini, S. Moortgat, L. Moreels, Q. Python, K. Skovpen, S. Tavernier, W. Van Doninck, P. Van Mulders, I. Van Parijs

Université Libre de Bruxelles, Bruxelles, Belgium

D. Beghin, B. Bilin, H. Brun, B. Clerboux, G. De Lentdecker, H. Delannoy, B. Dorney, G. Fasanella, L. Favart, R. Goldouzian, A. Grebenyuk, A.K. Kalsi, T. Lenzi, J. Luetic, T. Seva, E. Starling, C. Vander Velde, P. Vanlaer, D. Vannerom, R. Yonamine

Ghent University, Ghent, Belgium

T. Cornelis, D. Dobur, A. Fagot, M. Gul, I. Khvastunov², D. Poyraz, C. Roskas, D. Trocino, M. Tytgat, W. Verbeke, B. Vermassen, M. Vit, N. Zaganidis

Université Catholique de Louvain, Louvain-la-Neuve, Belgium

H. Bakhshiansohi, O. Bondu, S. Brochet, G. Bruno, C. Caputo, A. Caudron, P. David, S. De Visscher, C. Delaere, M. Delcourt, B. Francois, A. Giammanco, G. Krintiras, V. Lemaitre, A. Magitteri, A. Mertens, M. Musich, K. Piotrkowski, L. Quertenmont, A. Saggio, M. Vidal Marono, S. Wertz, J. Zobec

Centro Brasileiro de Pesquisas Fisicas, Rio de Janeiro, Brazil

W.L. Aldá Júnior, F.L. Alves, G.A. Alves, L. Brito, G. Correia Silva, C. Hensel, A. Moraes, M.E. Pol, P. Rebello Teles

Universidade do Estado do Rio de Janeiro, Rio de Janeiro, Brazil

E. Belchior Batista Das Chagas, W. Carvalho, J. Chinellato³, E. Coelho, E.M. Da Costa, G.G. Da Silveira⁴, D. De Jesus Damiao, S. Fonseca De Souza, H. Malbouisson, M. Medina Jaime⁵, M. Melo De Almeida, C. Mora Herrera, L. Mundim, H. Nogima, L.J. Sanchez Rosas, A. Santoro, A. Sznajder, M. Thiel, E.J. Tonelli Manganote³, F. Torres Da Silva De Araujo, A. Vilela Pereira

Universidade Estadual Paulista ^a, Universidade Federal do ABC ^b, São Paulo, Brazil

S. Ahuja^a, C.A. Bernardes^a, L. Calligaris^a, T.R. Fernandez Perez Tomei^a, E.M. Gregores^b, P.G. Mercadante^b, S.F. Novaes^a, Sandra S. Padula^a, D. Romero Abad^b, J.C. Ruiz Vargas^a

Institute for Nuclear Research and Nuclear Energy, Bulgarian Academy of Sciences, Sofia, Bulgaria

A. Aleksandrov, R. Hadjiiska, P. Iaydjiev, A. Marinov, M. Misheva, M. Rodozov, M. Shopova, G. Sultanov

University of Sofia, Sofia, Bulgaria

A. Dimitrov, L. Litov, B. Pavlov, P. Petkov

Beihang University, Beijing, China

W. Fang⁶, X. Gao⁶, L. Yuan

Institute of High Energy Physics, Beijing, China

M. Ahmad, J.G. Bian, G.M. Chen, H.S. Chen, M. Chen, Y. Chen, C.H. Jiang, D. Leggat, H. Liao, Z. Liu, F. Romeo, S.M. Shaheen, A. Spiezia, J. Tao, C. Wang, Z. Wang, E. Yazgan, H. Zhang, J. Zhao

State Key Laboratory of Nuclear Physics and Technology, Peking University, Beijing, China

Y. Ban, G. Chen, J. Li, Q. Li, S. Liu, Y. Mao, S.J. Qian, D. Wang, Z. Xu

Tsinghua University, Beijing, China

Y. Wang

Universidad de Los Andes, Bogota, Colombia

C. Avila, A. Cabrera, C.A. Carrillo Montoya, L.F. Chaparro Sierra, C. Florez, C.F. González Hernández, M.A. Segura Delgado

University of Split, Faculty of Electrical Engineering, Mechanical Engineering and Naval Architecture, Split, Croatia

B. Courbon, N. Godinovic, D. Lelas, I. Puljak, P.M. Ribeiro Cipriano, T. Sculac

University of Split, Faculty of Science, Split, Croatia

Z. Antunovic, M. Kovac

Institute Rudjer Boskovic, Zagreb, Croatia

V. Brigljevic, D. Ferencek, K. Kadija, B. Mesic, A. Starodumov⁷, T. Susa

University of Cyprus, Nicosia, Cyprus

M.W. Ather, A. Attikis, G. Mavromanolakis, J. Mousa, C. Nicolaou, F. Ptochos, P.A. Razis, H. Rykaczewski

Charles University, Prague, Czech Republic

M. Finger⁸, M. Finger Jr.⁸

Universidad San Francisco de Quito, Quito, Ecuador

E. Carrera Jarrin

Academy of Scientific Research and Technology of the Arab Republic of Egypt, Egyptian Network of High Energy Physics, Cairo, Egypt

A.A. Abdelalim^{9,10}, A. Ellithi Kamel¹¹, A. Mohamed¹⁰

National Institute of Chemical Physics and Biophysics, Tallinn, Estonia

S. Bhowmik, R.K. Dewanjee, M. Kadastik, L. Perrini, M. Raidal, C. Veelken

Department of Physics, University of Helsinki, Helsinki, Finland

P. Eerola, H. Kirschenmann, J. Pekkanen, M. Voutilainen

Helsinki Institute of Physics, Helsinki, Finland

J. Havukainen, J.K. Heikkilä, T. Järvinen, V. Karimäki, R. Kinnunen, T. Lampén, K. Lassila-Perini, S. Laurila, S. Lehti, T. Lindén, P. Luukka, T. Mäenpää, H. Siikonen, E. Tuominen, J. Tuominiemi

Lappeenranta University of Technology, Lappeenranta, Finland

T. Tuuva

IRFU, CEA, Université Paris-Saclay, Gif-sur-Yvette, France

M. Besancon, F. Couderc, M. Dejardin, D. Denegri, J.L. Faure, F. Ferri, S. Ganjour, S. Ghosh, A. Givernaud, P. Gras, G. Hamel de Monchenault, P. Jarry, C. Leloup, E. Locci, M. Machet, J. Malcles, G. Negro, J. Rander, A. Rosowsky, M.Ö. Sahin, M. Titov

Laboratoire Leprince-Ringuet, Ecole polytechnique, CNRS/IN2P3, Université Paris-Saclay, Palaiseau, France

A. Abdulsalam¹², C. Amendola, I. Antropov, S. Baffioni, F. Beaudette, P. Busson, L. Cadamuro, C. Charlot, R. Granier de Cassagnac, M. Jo, I. Kucher, S. Lisniak, A. Lobanov, J. Martin Blanco, M. Nguyen, C. Ochando, G. Ortona, P. Paganini, P. Pigard, R. Salerno, J.B. Sauvan, Y. Sirois, A.G. Stahl Leiton, Y. Yilmaz, A. Zabi, A. Zghiche

Université de Strasbourg, CNRS, IPHC UMR 7178, F-67000 Strasbourg, France

J.-L. Agram¹³, J. Andrea, D. Bloch, J.-M. Brom, E.C. Chabert, C. Collard, E. Conte¹³, X. Coubez, F. Drouhin¹³, J.-C. Fontaine¹³, D. Gelé, U. Goerlach, M. Jansová, P. Juillot, A.-C. Le Bihan, N. Tonon, P. Van Hove

Centre de Calcul de l'Institut National de Physique Nucleaire et de Physique des Particules, CNRS/IN2P3, Villeurbanne, France

S. Gadrat

Université de Lyon, Université Claude Bernard Lyon 1, CNRS-IN2P3, Institut de Physique Nucléaire de Lyon, Villeurbanne, France

S. Beauceron, C. Bernet, G. Boudoul, N. Chanon, R. Chierici, D. Contardo, P. Depasse, H. El Mamouni, J. Fay, L. Finco, S. Gascon, M. Gouzevitch, G. Grenier, B. Ille, F. Lagarde, I.B. Laktineh, H. Lattaud, M. Lethuillier, L. Mirabito, A.L. Pequegnot, S. Perries, A. Popov¹⁴, V. Sordini, M. Vander Donckt, S. Viret, S. Zhang

Georgian Technical University, Tbilisi, Georgia

A. Khvedelidze⁸

Tbilisi State University, Tbilisi, Georgia

Z. Tsamalaidze⁸

RWTH Aachen University, I. Physikalisches Institut, Aachen, Germany

C. Autermann, L. Feld, M.K. Kiesel, K. Klein, M. Lipinski, M. Preuten, M.P. Rauch, C. Schomakers, J. Schulz, M. Teroerde, B. Wittmer, V. Zhukov¹⁴

RWTH Aachen University, III. Physikalisches Institut A, Aachen, Germany

A. Albert, D. Duchardt, M. Endres, M. Erdmann, S. Erdweg, T. Esch, R. Fischer, A. Güth, T. Hebbeker, C. Heidemann, K. Hoepfner, S. Knutzen, M. Merschmeyer, A. Meyer, P. Millet, S. Mukherjee, T. Pook, M. Radziej, H. Reithler, M. Rieger, F. Scheuch, D. Teyssier, S. Thüer

RWTH Aachen University, III. Physikalisches Institut B, Aachen, Germany

G. Flügge, B. Kargoll, T. Kress, A. Künsken, T. Müller, A. Nehr Korn, A. Nowack, C. Pistone, O. Pooth, A. Stahl¹⁵

Deutsches Elektronen-Synchrotron, Hamburg, Germany

M. Aldaya Martin, T. Arndt, C. Asawatangtrakuldee, K. Beernaert, O. Behnke, U. Behrens, A. Bermúdez Martínez, A.A. Bin Anuar, K. Borras¹⁶, V. Botta, A. Campbell, P. Connor, C. Contreras-Campana, F. Costanza, V. Danilov, A. De Wit, C. Diez Pardos, D. Domínguez Damiani, G. Eckerlin, D. Eckstein, T. Eichhorn, A. Elwood, E. Eren, E. Gallo¹⁷, J. Garay Garcia, A. Geiser, J.M. Grados Luyando, A. Grohsjean, P. Gunnellini, M. Guthoff, A. Harb, J. Hauk, H. Jung, M. Kasemann, J. Keaveney, C. Kleinwort, J. Knolle, I. Korol, D. Krücker, W. Lange, A. Lelek, T. Lenz, K. Lipka, W. Lohmann¹⁸, R. Mankel, I.-A. Melzer-Pellmann, A.B. Meyer, M. Meyer, M. Missiroli, G. Mittag, J. Mnich, A. Mussgiller, D. Pitzl, A. Raspereza, M. Savitskyi, P. Saxena, R. Shevchenko, N. Stefaniuk, H. Tholen, G.P. Van Onsem, R. Walsh, Y. Wen, K. Wichmann, C. Wissing, O. Zenaiev

University of Hamburg, Hamburg, Germany

R. Aggleton, S. Bein, V. Blobel, M. Centis Vignali, T. Dreyer, E. Garutti, D. Gonzalez, J. Haller, A. Hinzmann, M. Hoffmann, A. Karavdina, G. Kasieczka, R. Klanner, R. Kogler, N. Kovalchuk, S. Kurz, V. Kutzner, J. Lange, D. Marconi, J. Multhaupt, M. Niedziela, D. Nowatschin, T. Peiffer, A. Perieanu, A. Reimers, C. Scharf, P. Schleper, A. Schmidt, S. Schumann, J. Schwandt, J. Sonneveld, H. Stadie, G. Steinbrück, F.M. Stober, M. Stöver, D. Troendle, E. Usai, A. Vanhoefer, B. Vormwald

Institut für Experimentelle Teilchenphysik, Karlsruhe, Germany

M. Akbiyik, C. Barth, M. Baselga, S. Baur, E. Butz, R. Caspart, T. Chwalek, F. Colombo, W. De Boer, A. Dierlamm, N. Faltermann, B. Freund, R. Friese, M. Giffels, M.A. Harrendorf, F. Hartmann¹⁵, S.M. Heindl, U. Husemann, F. Kassel¹⁵, S. Kudella, H. Mildner, M.U. Mozer, Th. Müller, M. Plagge, G. Quast, K. Rabbertz, M. Schröder, I. Shvetsov, G. Sieber, H.J. Simonis, R. Ulrich, S. Wayand, M. Weber, T. Weiler, S. Williamson, C. Wöhrmann, R. Wolf

Institute of Nuclear and Particle Physics (INPP), NCSR Demokritos, Aghia Paraskevi, Greece

G. Anagnostou, G. Daskalakis, T. Gerasis, A. Kyriakis, D. Loukas, I. Topsis-Giotis

National and Kapodistrian University of Athens, Athens, Greece

G. Karathanasis, S. Kesisoglou, A. Panagiotou, N. Saoulidou, E. Tziaferi

National Technical University of Athens, Athens, Greece

K. Kousouris, I. Papakrivopoulos

University of Ioánnina, Ioánnina, Greece

I. Evangelou, C. Foudas, P. Gianneios, P. Katsoulis, P. Kokkas, S. Mallios, N. Manthos, I. Papadopoulos, E. Paradas, J. Strologas, F.A. Triantis, D. Tsitsonis

MTA-ELTE Lendület CMS Particle and Nuclear Physics Group, Eötvös Loránd University, Budapest, Hungary

M. Csanad, N. Filipovic, G. Pasztor, O. Surányi, G.I. Veres

Wigner Research Centre for Physics, Budapest, Hungary

G. Bencze, C. Hajdu, D. Horvath¹⁹, Á. Hunyadi, F. Sikler, T.Á. Vámi, V. Veszpremi, G. Vesztergombi[†]

Institute of Nuclear Research ATOMKI, Debrecen, Hungary

N. Beni, S. Czellar, J. Karancsi²¹, A. Makovec, J. Molnar, Z. Szillasi

Institute of Physics, University of Debrecen, Debrecen, Hungary

M. Bartók²⁰, P. Raics, Z.L. Trocsanyi, B. Ujvari

Indian Institute of Science (IISc), Bangalore, India

S. Choudhury, J.R. Komaragiri

National Institute of Science Education and Research, Bhubaneswar, IndiaS. Bahinipati²², P. Mal, K. Mandal, A. Nayak²³, D.K. Sahoo²², S.K. Swain**Panjab University, Chandigarh, India**

S. Bansal, S.B. Beri, V. Bhatnagar, S. Chauhan, R. Chawla, N. Dhingra, R. Gupta, A. Kaur, M. Kaur, S. Kaur, R. Kumar, P. Kumari, M. Lohan, A. Mehta, S. Sharma, J.B. Singh, G. Walia

University of Delhi, Delhi, India

A. Bhardwaj, B.C. Choudhary, R.B. Garg, S. Keshri, A. Kumar, Ashok Kumar, S. Malhotra, M. Naimuddin, K. Ranjan, Aashaq Shah, R. Sharma

Saha Institute of Nuclear Physics, HBNI, Kolkata, IndiaR. Bhardwaj²⁴, R. Bhattacharya, S. Bhattacharya, U. Bhawandeep²⁴, D. Bhowmik, S. Dey, S. Dutt²⁴, S. Dutta, S. Ghosh, N. Majumdar, K. Mondal, S. Mukhopadhyay, S. Nandan, A. Purohit, P.K. Rout, A. Roy, S. Roy Chowdhury, S. Sarkar, M. Sharan, B. Singh, S. Thakur²⁴**Indian Institute of Technology Madras, Madras, India**

P.K. Behera

Bhabha Atomic Research Centre, Mumbai, IndiaR. Chudasama, D. Dutta, V. Jha, V. Kumar, A.K. Mohanty¹⁵, P.K. Netrakanti, L.M. Pant, P. Shukla, A. Topkar**Tata Institute of Fundamental Research-A, Mumbai, India**

T. Aziz, S. Dugad, B. Mahakud, S. Mitra, G.B. Mohanty, N. Sur, B. Sutar

Tata Institute of Fundamental Research-B, Mumbai, IndiaS. Banerjee, S. Bhattacharya, S. Chatterjee, P. Das, M. Guchait, Sa. Jain, S. Kumar, M. Maity²⁵, G. Majumder, K. Mazumdar, N. Sahoo, T. Sarkar²⁵, N. Wickramage²⁶**Indian Institute of Science Education and Research (IISER), Pune, India**

S. Chauhan, S. Dube, V. Hegde, A. Kapoor, K. Kothekar, S. Pandey, A. Rane, S. Sharma

Institute for Research in Fundamental Sciences (IPM), Tehran, IranS. Chenarani²⁷, E. Eskandari Tadavani, S.M. Etesami²⁷, M. Khakzad, M. Mohammadi Najafabadi, M. Naseri, S. Paktinat Mehdiabadi²⁸, F. Rezaei Hosseinabadi, B. Safarzadeh²⁹, M. Zeinali**University College Dublin, Dublin, Ireland**

M. Felcini, M. Grunewald

INFN Sezione di Bari ^a, Università di Bari ^b, Politecnico di Bari ^c, Bari, ItalyM. Abbrescia^{a,b}, C. Calabria^{a,b}, A. Colaleo^a, D. Creanza^{a,c}, L. Cristella^{a,b}, N. De Filippis^{a,c}, M. De Palma^{a,b}, A. Di Florio^{a,b}, F. Errico^{a,b}, L. Fiore^a, A. Gelmi^{a,b}, G. Iaselli^{a,c}, S. Lezki^{a,b}, G. Maggi^{a,c}, M. Maggi^a, B. Marangelli^{a,b}, G. Miniello^{a,b}, S. My^{a,b}, S. Nuzzo^{a,b}, A. Pompili^{a,b}, G. Pugliese^{a,c}, R. Radogna^a, A. Ranieri^a, G. Selvaggi^{a,b}, A. Sharma^a, L. Silvestris^{a,15}, R. Venditti^a, P. Verwilligen^a, G. Zito^a**INFN Sezione di Bologna ^a, Università di Bologna ^b, Bologna, Italy**G. Abbiendi^a, C. Battilana^{a,b}, D. Bonacorsi^{a,b}, L. Borgonovi^{a,b}, S. Braibant-Giacomelli^{a,b}, L. Brigliadori^{a,b}, R. Campanini^{a,b}, P. Capiluppi^{a,b}, A. Castro^{a,b}, F.R. Cavallo^a, S.S. Chhibra^{a,b}, G. Codispoti^{a,b}, M. Cuffiani^{a,b}, G.M. Dallavalle^a, F. Fabbri^a, A. Fanfani^{a,b}, D. Fasanella^{a,b},

P. Giacomelli^a, C. Grandi^a, L. Guiducci^{a,b}, F. Iemmi, S. Marcellini^a, G. Masetti^a, A. Montanari^a, F.L. Navarria^{a,b}, A. Perrotta^a, T. Rovelli^{a,b}, G.P. Siroli^{a,b}, N. Tosi^a

INFN Sezione di Catania^a, Università di Catania^b, Catania, Italy

S. Albergo^{a,b}, S. Costa^{a,b}, A. Di Mattia^a, F. Giordano^{a,b}, R. Potenza^{a,b}, A. Tricomi^{a,b}, C. Tuve^{a,b}

INFN Sezione di Firenze^a, Università di Firenze^b, Firenze, Italy

G. Barbagli^a, K. Chatterjee^{a,b}, V. Ciulli^{a,b}, C. Civinini^a, R. D'Alessandro^{a,b}, E. Focardi^{a,b}, G. Latino, P. Lenzi^{a,b}, M. Meschini^a, S. Paoletti^a, L. Russo^{a,30}, G. Sguazzoni^a, D. Strom^a, L. Viliani^a

INFN Laboratori Nazionali di Frascati, Frascati, Italy

L. Benussi, S. Bianco, F. Fabbri, D. Piccolo, F. Primavera¹⁵

INFN Sezione di Genova^a, Università di Genova^b, Genova, Italy

V. Calvelli^{a,b}, F. Ferro^a, F. Ravera^{a,b}, E. Robutti^a, S. Tosi^{a,b}

INFN Sezione di Milano-Bicocca^a, Università di Milano-Bicocca^b, Milano, Italy

A. Benaglia^a, A. Beschi^b, L. Brianza^{a,b}, F. Brivio^{a,b}, V. Ciriolo^{a,b,15}, M.E. Dinardo^{a,b}, S. Fiorendi^{a,b}, S. Gennai^a, A. Ghezzi^{a,b}, P. Govoni^{a,b}, M. Malberti^{a,b}, S. Malvezzi^a, R.A. Manzoni^{a,b}, D. Menasce^a, L. Moroni^a, M. Paganoni^{a,b}, K. Pauwels^{a,b}, D. Pedrini^a, S. Pigazzini^{a,b,31}, S. Ragazzi^{a,b}, T. Tabarelli de Fatis^{a,b}

INFN Sezione di Napoli^a, Università di Napoli 'Federico II'^b, Napoli, Italy, Università della Basilicata^c, Potenza, Italy, Università G. Marconi^d, Roma, Italy

S. Buontempo^a, N. Cavallo^{a,c}, S. Di Guida^{a,d,15}, F. Fabozzi^{a,c}, F. Fienga^{a,b}, G. Galati^{a,b}, A.O.M. Iorio^{a,b}, W.A. Khan^a, L. Lista^a, S. Meola^{a,d,15}, P. Paolucci^{a,15}, C. Sciacca^{a,b}, F. Thyssen^a, E. Voevodina^{a,b}

INFN Sezione di Padova^a, Università di Padova^b, Padova, Italy, Università di Trento^c, Trento, Italy

P. Azzi^a, N. Bacchetta^a, L. Benato^{a,b}, D. Bisello^{a,b}, A. Boletti^{a,b}, R. Carlin^{a,b}, A. Carvalho Antunes De Oliveira^{a,b}, P. Checchia^a, M. Dall'Osso^{a,b}, P. De Castro Manzano^a, T. Dorigo^a, U. Dosselli^a, F. Gasparini^{a,b}, U. Gasparini^{a,b}, A. Gozzelino^a, S. Lacaprara^a, P. Lujan, M. Margoni^{a,b}, A.T. Meneguzzo^{a,b}, N. Pozzobon^{a,b}, P. Ronchese^{a,b}, R. Rossin^{a,b}, F. Simonetto^{a,b}, A. Tiko, E. Torassa^a, M. Zanetti^{a,b}, P. Zotto^{a,b}

INFN Sezione di Pavia^a, Università di Pavia^b, Pavia, Italy

A. Braghieri^a, A. Magnani^a, P. Montagna^{a,b}, S.P. Ratti^{a,b}, V. Re^a, M. Ressegotti^{a,b}, C. Riccardi^{a,b}, P. Salvini^a, I. Vai^{a,b}, P. Vitulo^{a,b}

INFN Sezione di Perugia^a, Università di Perugia^b, Perugia, Italy

L. Alunni Solestizi^{a,b}, M. Biasini^{a,b}, G.M. Bilei^a, C. Cecchi^{a,b}, D. Ciangottini^{a,b}, L. Fanò^{a,b}, P. Lariccia^{a,b}, R. Leonardi^{a,b}, E. Manoni^a, G. Mantovani^{a,b}, V. Mariani^{a,b}, M. Menichelli^a, A. Rossi^{a,b}, A. Santocchia^{a,b}, D. Spiga^a

INFN Sezione di Pisa^a, Università di Pisa^b, Scuola Normale Superiore di Pisa^c, Pisa, Italy

K. Androsov^a, P. Azzurri^a, G. Bagliesi^a, L. Bianchini^a, T. Boccali^a, L. Borrello, R. Castaldi^a, M.A. Ciocci^{a,b}, R. Dell'Orso^a, G. Fedi^a, L. Giannini^{a,c}, A. Giassi^a, M.T. Grippo^a, F. Ligabue^{a,c}, T. Lomtadze^a, E. Manca^{a,c}, G. Mandorli^{a,c}, A. Messineo^{a,b}, F. Palla^a, A. Rizzi^{a,b}, P. Spagnolo^a, R. Tenchini^a, G. Tonelli^{a,b}, A. Venturi^a, P.G. Verdini^a

INFN Sezione di Roma^a, Sapienza Università di Roma^b, Rome, Italy

L. Barone^{a,b}, F. Cavallari^a, M. Cipriani^{a,b}, N. Daci^a, D. Del Re^{a,b}, E. Di Marco^{a,b}, M. Diemoz^a,

S. Gelli^{a,b}, E. Longo^{a,b}, B. Marzocchi^{a,b}, P. Meridiani^a, G. Organtini^{a,b}, F. Pandolfi^a, R. Paramatti^{a,b}, F. Preiato^{a,b}, S. Rahatlou^{a,b}, C. Rovelli^a, F. Santanastasio^{a,b}

INFN Sezione di Torino^a, Università di Torino^b, Torino, Italy, Università del Piemonte Orientale^c, Novara, Italy

N. Amapane^{a,b}, R. Arcidiacono^{a,c}, S. Argiro^{a,b}, M. Arneodo^{a,c}, N. Bartosik^a, R. Bellan^{a,b}, C. Biino^a, N. Cartiglia^a, R. Castello^{a,b}, F. Cenna^{a,b}, M. Costa^{a,b}, R. Covarelli^{a,b}, A. Degano^{a,b}, N. Demaria^a, B. Kiani^{a,b}, C. Mariotti^a, S. Maselli^a, E. Migliore^{a,b}, V. Monaco^{a,b}, E. Monteil^{a,b}, M. Monteno^a, M.M. Obertino^{a,b}, L. Pacher^{a,b}, N. Pastrone^a, M. Pelliccioni^a, G.L. Pinna Angioni^{a,b}, A. Romero^{a,b}, M. Ruspa^{a,c}, R. Sacchi^{a,b}, K. Shchelina^{a,b}, V. Sola^a, A. Solano^{a,b}, A. Staiano^a

INFN Sezione di Trieste^a, Università di Trieste^b, Trieste, Italy

S. Belforte^a, M. Casarsa^a, F. Cossutti^a, G. Della Ricca^{a,b}, A. Zanetti^a

Kyungpook National University

D.H. Kim, G.N. Kim, M.S. Kim, J. Lee, S. Lee, S.W. Lee, C.S. Moon, Y.D. Oh, S. Sekmen, D.C. Son, Y.C. Yang

Chonnam National University, Institute for Universe and Elementary Particles, Kwangju, Korea

H. Kim, D.H. Moon, G. Oh

Hanyang University, Seoul, Korea

J.A. Brochero Cifuentes, J. Goh, T.J. Kim

Korea University, Seoul, Korea

S. Cho, S. Choi, Y. Go, D. Gyun, S. Ha, B. Hong, Y. Jo, Y. Kim, K. Lee, K.S. Lee, S. Lee, J. Lim, S.K. Park, Y. Roh

Seoul National University, Seoul, Korea

J. Almond, J. Kim, J.S. Kim, H. Lee, K. Lee, K. Nam, S.B. Oh, B.C. Radburn-Smith, S.h. Seo, U.K. Yang, H.D. Yoo, G.B. Yu

University of Seoul, Seoul, Korea

H. Kim, J.H. Kim, J.S.H. Lee, I.C. Park

Sungkyunkwan University, Suwon, Korea

Y. Choi, C. Hwang, J. Lee, I. Yu

Vilnius University, Vilnius, Lithuania

V. Dudenas, A. Juodagalvis, J. Vaitkus

National Centre for Particle Physics, Universiti Malaya, Kuala Lumpur, Malaysia

I. Ahmed, Z.A. Ibrahim, M.A.B. Md Ali³², F. Mohamad Idris³³, W.A.T. Wan Abdullah, M.N. Yusli, Z. Zolkapli

Centro de Investigacion y de Estudios Avanzados del IPN, Mexico City, Mexico

Duran-Osuna, M. C., H. Castilla-Valdez, E. De La Cruz-Burelo, Ramirez-Sanchez, G., I. Heredia-De La Cruz³⁴, Rabadan-Trejo, R. I., R. Lopez-Fernandez, J. Mejia Guisao, Reyes-Almanza, R, A. Sanchez-Hernandez

Universidad Iberoamericana, Mexico City, Mexico

S. Carrillo Moreno, C. Oropeza Barrera, F. Vazquez Valencia

Benemerita Universidad Autonoma de Puebla, Puebla, Mexico

J. Eysermans, I. Pedraza, H.A. Salazar Ibarguen, C. Uribe Estrada

Universidad Autónoma de San Luis Potosí, San Luis Potosí, Mexico

A. Morelos Pineda

University of Auckland, Auckland, New Zealand

D. Krofcheck

University of Canterbury, Christchurch, New Zealand

S. Bheesette, P.H. Butler

National Centre for Physics, Quaid-I-Azam University, Islamabad, Pakistan

A. Ahmad, M. Ahmad, Q. Hassan, H.R. Hoorani, A. Saddique, M.A. Shah, M. Shoaib, M. Waqas

National Centre for Nuclear Research, Swierk, Poland

H. Bialkowska, M. Bluj, B. Boimska, T. Frueboes, M. Górski, M. Kazana, K. Nawrocki, M. Szleper, P. Traczyk, P. Zalewski

Institute of Experimental Physics, Faculty of Physics, University of Warsaw, Warsaw, Poland

K. Bunkowski, A. Byszuk³⁵, K. Doroba, A. Kalinowski, M. Konecki, J. Krolikowski, M. Misiura, M. Olszewski, A. Pyskir, M. Walczak

Laboratório de Instrumentação e Física Experimental de Partículas, Lisboa, Portugal

P. Bargassa, C. Beirão Da Cruz E Silva, A. Di Francesco, P. Faccioli, B. Galinhas, M. Gallinaro, J. Hollar, N. Leonardo, L. Lloret Iglesias, M.V. Nemallapudi, J. Seixas, G. Strong, O. Toldaiev, D. Vadrucio, J. Varela

Joint Institute for Nuclear Research, Dubna, Russia

V. Alexakhin, A. Golunov, I. Golutvin, N. Gorbounov, I. Gorbunov, A. Kamenev, V. Karjavin, A. Lanev, A. Malakhov, V. Matveev^{36,37}, P. Moisenz, V. Palichik, V. Perelygin, M. Savina, S. Shmatov, S. Shulha, N. Skatchkov, V. Smirnov, A. Zarubin

Petersburg Nuclear Physics Institute, Gatchina (St. Petersburg), Russia

Y. Ivanov, V. Kim³⁸, E. Kuznetsova³⁹, P. Levchenko, V. Murzin, V. Oreshkin, I. Smirnov, D. Sosnov, V. Sulimov, L. Uvarov, S. Vavilov, A. Vorobyev

Institute for Nuclear Research, Moscow, Russia

Yu. Andreev, A. Dermenev, S. Gninenko, N. Golubev, A. Karneyeu, M. Kirsanov, N. Krasnikov, A. Pashenkov, D. Tlisov, A. Toropin

Institute for Theoretical and Experimental Physics, Moscow, Russia

V. Epshteyn, V. Gavrillov, N. Lychkovskaya, V. Popov, I. Pozdnyakov, G. Safronov, A. Spiridonov, A. Stepenov, V. Stolin, M. Toms, E. Vlasov, A. Zhokin

Moscow Institute of Physics and Technology, Moscow, Russia

T. Aushev, A. Bylinkin³⁷

National Research Nuclear University 'Moscow Engineering Physics Institute' (MEPhI), Moscow, Russia

R. Chistov⁴⁰, M. Danilov⁴⁰, P. Parygin, D. Philippov, S. Polikarpov, E. Tarkovskii

P.N. Lebedev Physical Institute, Moscow, Russia

V. Andreev, M. Azarkin³⁷, I. Dremin³⁷, M. Kirakosyan³⁷, S.V. Rusakov, A. Terkulov

Skobeltsyn Institute of Nuclear Physics, Lomonosov Moscow State University, Moscow, Russia

A. Baskakov, A. Belyaev, E. Boos, V. Bunichev, M. Dubinin⁴¹, L. Dudko, A. Ershov, A. Gribushin, V. Klyukhin, O. Kodolova, I. Lokhtin, I. Miagkov, S. Obraztsov, S. Petrushanko, V. Savrin

Novosibirsk State University (NSU), Novosibirsk, Russia

V. Blinov⁴², D. Shtol⁴², Y. Skovpen⁴²

State Research Center of Russian Federation, Institute for High Energy Physics of NRC " Kurchatov Institute", Protvino, Russia

I. Azhgirey, I. Bayshev, S. Bitioukov, D. Elumakhov, A. Godizov, V. Kachanov, A. Kalinin, D. Konstantinov, P. Mandrik, V. Petrov, R. Ryutin, A. Sobol, S. Troshin, N. Tyurin, A. Uzunian, A. Volkov

National Research Tomsk Polytechnic University, Tomsk, Russia

A. Babaev

University of Belgrade, Faculty of Physics and Vinca Institute of Nuclear Sciences, Belgrade, Serbia

P. Adzic⁴³, P. Cirkovic, D. Devetak, M. Dordevic, J. Milosevic

Centro de Investigaciones Energéticas Medioambientales y Tecnológicas (CIEMAT), Madrid, Spain

J. Alcaraz Maestre, A. Álvarez Fernández, I. Bachiller, M. Barrio Luna, M. Cerrada, N. Colino, B. De La Cruz, A. Delgado Peris, C. Fernandez Bedoya, J.P. Fernández Ramos, J. Flix, M.C. Fouz, O. Gonzalez Lopez, S. Goy Lopez, J.M. Hernandez, M.I. Josa, D. Moran, A. Pérez-Calero Yzquierdo, J. Puerta Pelayo, I. Redondo, L. Romero, M.S. Soares, A. Triossi

Universidad Autónoma de Madrid, Madrid, Spain

C. Albajar, J.F. de Trocóniz

Universidad de Oviedo, Oviedo, Spain

J. Cuevas, C. Erice, J. Fernandez Menendez, S. Folgueras, I. Gonzalez Caballero, J.R. González Fernández, E. Palencia Cortezon, S. Sanchez Cruz, P. Vischia, J.M. Vizán García

Instituto de Física de Cantabria (IFCA), CSIC-Universidad de Cantabria, Santander, Spain

I.J. Cabrillo, A. Calderon, B. Chazin Quero, J. Duarte Campderros, M. Fernandez, P.J. Fernández Manteca, A. García Alonso, J. Garcia-Ferrero, G. Gomez, A. Lopez Virto, J. Marco, C. Martinez Rivero, P. Martinez Ruiz del Arbol, F. Matorras, J. Piedra Gomez, C. Prieels, T. Rodrigo, A. Ruiz-Jimeno, L. Scodellaro, N. Trevisani, I. Vila, R. Vilar Cortabitarte

CERN, European Organization for Nuclear Research, Geneva, Switzerland

D. Abbaneo, B. Akgun, E. Auffray, P. Baillon, A.H. Ball, D. Barney, J. Bendavid, M. Bianco, A. Bocci, C. Botta, T. Camporesi, M. Cepeda, G. Cerminara, E. Chapon, Y. Chen, D. d'Enterria, A. Dabrowski, V. Daponte, A. David, M. De Gruttola, A. De Roeck, N. Deelen, M. Dobson, T. du Pree, M. Dünser, N. Dupont, A. Elliott-Peisert, P. Everaerts, F. Fallavollita⁴⁴, G. Franzoni, J. Fulcher, W. Funk, D. Gigi, A. Gilbert, K. Gill, F. Glege, D. Gulhan, J. Hegeman, V. Innocente, A. Jafari, P. Janot, O. Karacheban¹⁸, J. Kieseler, V. Knünz, A. Kornmayer, M. Kramer¹, C. Lange, P. Lecoq, C. Lourenço, M.T. Lucchini, L. Malgeri, M. Mannelli, A. Martelli, F. Meijers, J.A. Merlin, S. Mersi, E. Meschi, P. Milenovic⁴⁵, F. Moortgat, M. Mulders, H. Neugebauer, J. Ngadiuba, S. Orfanelli, L. Orsini, F. Pantaleo¹⁵, L. Pape, E. Perez, M. Peruzzi, A. Petrilli, G. Petrucciani, A. Pfeiffer, M. Pierini, F.M. Pitters, D. Rabady, A. Racz, T. Reis, G. Rolandi⁴⁶, M. Rovere, H. Sakulin, C. Schäfer, C. Schwick, M. Seidel, M. Selvaggi, A. Sharma, P. Silva,

P. Sphicas⁴⁷, A. Stakia, J. Steggemann, M. Stoye, M. Tosi, D. Treille, A. Tsirou, V. Veckalns⁴⁸, M. Verweij, W.D. Zeuner

Paul Scherrer Institut, Villigen, Switzerland

W. Bertl[†], L. Caminada⁴⁹, K. Deiters, W. Erdmann, R. Horisberger, Q. Ingram, H.C. Kaestli, D. Kotlinski, U. Langenegger, T. Rohe, S.A. Wiederkehr

ETH Zurich - Institute for Particle Physics and Astrophysics (IPA), Zurich, Switzerland

M. Backhaus, L. Bäni, P. Berger, B. Casal, N. Chernyavskaya, G. Dissertori, M. Dittmar, M. Donegà, C. Dorfer, C. Grab, C. Heidegger, D. Hits, J. Hoss, T. Klijnsma, W. Luster, M. Marionneau, M.T. Meinhard, D. Meister, F. Micheli, P. Musella, F. Nessi-Tedaldi, J. Pata, F. Pauss, G. Perrin, L. Perrozzi, M. Quittnat, M. Reichmann, D. Ruini, D.A. Sanz Becerra, M. Schönenberger, L. Shchutska, V.R. Tavolaro, K. Theofilatos, M.L. Vesterbacka Olsson, R. Wallny, D.H. Zhu

Universität Zürich, Zurich, Switzerland

T.K. Aarrestad, C. Amsler⁵⁰, D. Brzhechko, M.F. Canelli, A. De Cosa, R. Del Burgo, S. Donato, C. Galloni, T. Hreus, B. Kilminster, I. Neutelings, D. Pinna, G. Rauco, P. Robmann, D. Salerno, K. Schweiger, C. Seitz, Y. Takahashi, A. Zucchetta

National Central University, Chung-Li, Taiwan

V. Candelise, Y.H. Chang, K.y. Cheng, T.H. Doan, Sh. Jain, R. Khurana, C.M. Kuo, W. Lin, A. Pozdnyakov, S.S. Yu

National Taiwan University (NTU), Taipei, Taiwan

P. Chang, Y. Chao, K.F. Chen, P.H. Chen, F. Fiori, W.-S. Hou, Y. Hsiung, Arun Kumar, Y.F. Liu, R.-S. Lu, E. Paganis, A. Psallidas, A. Steen, J.f. Tsai

Chulalongkorn University, Faculty of Science, Department of Physics, Bangkok, Thailand

B. Asavapibhop, K. Kovitanggoon, G. Singh, N. Srimanobhas

Çukurova University, Physics Department, Science and Art Faculty, Adana, Turkey

A. Bat, F. Boran, S. Cerci⁵¹, S. Damarseckin, Z.S. Demiroglu, C. Dozen, I. Dumanoglu, S. Girgis, G. Gokbulut, Y. Guler, I. Hos⁵², E.E. Kangal⁵³, O. Kara, A. Kayis Topaksu, U. Kiminsu, M. Oglakci, G. Onengut, K. Ozdemir⁵⁴, D. Sunar Cerci⁵¹, B. Tali⁵¹, U.G. Tok, S. Turkcapar, I.S. Zorbakir, C. Zorbilmez

Middle East Technical University, Physics Department, Ankara, Turkey

G. Karapinar⁵⁵, K. Ocalan⁵⁶, M. Yalvac, M. Zeyrek

Bogazici University, Istanbul, Turkey

I.O. Atakisi, E. Gülmez, M. Kaya⁵⁷, O. Kaya⁵⁸, S. Tekten, E.A. Yetkin⁵⁹

Istanbul Technical University, Istanbul, Turkey

M.N. Agaras, S. Atay, A. Cakir, K. Cankocak, Y. Komurcu

Institute for Scintillation Materials of National Academy of Science of Ukraine, Kharkov, Ukraine

B. Grynyov

National Scientific Center, Kharkov Institute of Physics and Technology, Kharkov, Ukraine

L. Levchuk

University of Bristol, Bristol, United Kingdom

F. Ball, L. Beck, J.J. Brooke, D. Burns, E. Clement, D. Cussans, O. Davignon, H. Flacher,

J. Goldstein, G.P. Heath, H.F. Heath, L. Kreczko, D.M. Newbold⁶⁰, S. Paramesvaran, T. Sakuma, S. Seif El Nasr-storey, D. Smith, V.J. Smith

Rutherford Appleton Laboratory, Didcot, United Kingdom

K.W. Bell, A. Belyaev⁶¹, C. Brew, R.M. Brown, D. Cieri, D.J.A. Cockerill, J.A. Coughlan, K. Harder, S. Harper, J. Linacre, E. Olaiya, D. Petyt, C.H. Shepherd-Themistocleous, A. Thea, I.R. Tomalin, T. Williams, W.J. Womersley

Imperial College, London, United Kingdom

G. Auzinger, R. Bainbridge, P. Bloch, J. Borg, S. Breeze, O. Buchmuller, A. Bundock, S. Casasso, D. Colling, L. Corpe, P. Dauncey, G. Davies, M. Della Negra, R. Di Maria, Y. Haddad, G. Hall, G. Iles, T. James, M. Komm, R. Lane, C. Laner, L. Lyons, A.-M. Magnan, S. Malik, L. Mastrolorenzo, T. Matsushita, J. Nash⁶², A. Nikitenko⁷, V. Palladino, M. Pesaresi, A. Richards, A. Rose, E. Scott, C. Seez, A. Shtipliyski, T. Strebler, S. Summers, A. Tapper, K. Uchida, M. Vazquez Acosta⁶³, T. Virdee¹⁵, N. Wardle, D. Winterbottom, J. Wright, S.C. Zenz

Brunel University, Uxbridge, United Kingdom

J.E. Cole, P.R. Hobson, A. Khan, P. Kyberd, A. Morton, I.D. Reid, L. Teodorescu, S. Zahid

Baylor University, Waco, USA

A. Borzou, K. Call, J. Dittmann, K. Hatakeyama, H. Liu, N. Pastika, C. Smith

Catholic University of America, Washington DC, USA

R. Bartek, A. Dominguez

The University of Alabama, Tuscaloosa, USA

A. Buccilli, S.I. Cooper, C. Henderson, P. Rumerio, C. West

Boston University, Boston, USA

D. Arcaro, A. Avetisyan, T. Bose, D. Gastler, D. Rankin, C. Richardson, J. Rohlf, L. Sulak, D. Zou

Brown University, Providence, USA

G. Benelli, D. Cutts, M. Hadley, J. Hakala, U. Heintz, J.M. Hogan⁶⁴, K.H.M. Kwok, E. Laird, G. Landsberg, J. Lee, Z. Mao, M. Narain, J. Pazzini, S. Piperov, S. Sagir, R. Syarif, D. Yu

University of California, Davis, Davis, USA

R. Band, C. Brainerd, R. Breedon, D. Burns, M. Calderon De La Barca Sanchez, M. Chertok, J. Conway, R. Conway, P.T. Cox, R. Erbacher, C. Flores, G. Funk, W. Ko, R. Lander, C. Mclean, M. Mulhearn, D. Pellett, J. Pilot, S. Shalhout, M. Shi, J. Smith, D. Stolp, D. Taylor, K. Tos, M. Tripathi, Z. Wang, F. Zhang

University of California, Los Angeles, USA

M. Bachtis, C. Bravo, R. Cousins, A. Dasgupta, A. Florent, J. Hauser, M. Ignatenko, N. Mccoll, S. Regnard, D. Saltzberg, C. Schnaible, V. Valuev

University of California, Riverside, Riverside, USA

E. Bouvier, K. Burt, R. Clare, J. Ellison, J.W. Gary, S.M.A. Ghiasi Shirazi, G. Hanson, G. Karapostoli, E. Kennedy, F. Lacroix, O.R. Long, M. Olmedo Negrete, M.I. Paneva, W. Si, L. Wang, H. Wei, S. Wimpenny, B. R. Yates

University of California, San Diego, La Jolla, USA

J.G. Branson, S. Cittolin, M. Derdzinski, R. Gerosa, D. Gilbert, B. Hashemi, A. Holzner, D. Klein, G. Kole, V. Krutelyov, J. Letts, M. Masciovecchio, D. Olivito, S. Padhi, M. Pieri, M. Sani, V. Sharma, S. Simon, M. Tadel, A. Vartak, S. Wasserbaech⁶⁵, J. Wood, F. Würthwein, A. Yagil, G. Zevi Della Porta

University of California, Santa Barbara - Department of Physics, Santa Barbara, USA

N. Amin, R. Bhandari, J. Bradmiller-Feld, C. Campagnari, M. Citron, A. Dishaw, V. Dutta, M. Franco Sevilla, L. Gouskos, R. Heller, J. Incandela, A. Ovcharova, H. Qu, J. Richman, D. Stuart, I. Suarez, J. Yoo

California Institute of Technology, Pasadena, USA

D. Anderson, A. Bornheim, J. Bunn, J.M. Lawhorn, H.B. Newman, T. Q. Nguyen, C. Pena, M. Spiropulu, J.R. Vlimant, R. Wilkinson, S. Xie, Z. Zhang, R.Y. Zhu

Carnegie Mellon University, Pittsburgh, USA

M.B. Andrews, T. Ferguson, T. Mudholkar, M. Paulini, J. Russ, M. Sun, H. Vogel, I. Vorobiev, M. Weinberg

University of Colorado Boulder, Boulder, USA

J.P. Cumalat, W.T. Ford, F. Jensen, A. Johnson, M. Krohn, S. Leontsinis, E. MacDonald, T. Mulholland, K. Stenson, K.A. Ulmer, S.R. Wagner

Cornell University, Ithaca, USA

J. Alexander, J. Chaves, Y. Cheng, J. Chu, A. Datta, K. Mcdermott, N. Mirman, J.R. Patterson, D. Quach, A. Rinkevicius, A. Ryd, L. Skinnari, L. Soffi, S.M. Tan, Z. Tao, J. Thom, J. Tucker, P. Wittich, M. Zientek

Fermi National Accelerator Laboratory, Batavia, USA

S. Abdullin, M. Albrow, M. Alyari, G. Apollinari, A. Apresyan, A. Apyan, S. Banerjee, L.A.T. Bauerdick, A. Beretvas, J. Berryhill, P.C. Bhat, G. Bolla[†], K. Burkett, J.N. Butler, A. Canepa, G.B. Cerati, H.W.K. Cheung, F. Chlebana, M. Cremonesi, J. Duarte, V.D. Elvira, J. Freeman, Z. Gecse, E. Gottschalk, L. Gray, D. Green, S. Grünendahl, O. Gutsche, J. Hanlon, R.M. Harris, S. Hasegawa, J. Hirschauer, Z. Hu, B. Jayatilaka, S. Jindariani, M. Johnson, U. Joshi, B. Klima, M.J. Kortelainen, B. Kreis, S. Lammel, D. Lincoln, R. Lipton, M. Liu, T. Liu, R. Lopes De Sá, J. Lykken, K. Maeshima, N. Magini, J.M. Marraffino, D. Mason, P. McBride, P. Merkel, S. Mrenna, S. Nahn, V. O'Dell, K. Pedro, O. Prokofyev, G. Rakness, L. Ristori, A. Savoy-Navarro⁶⁶, B. Schneider, E. Sexton-Kennedy, A. Soha, W.J. Spalding, L. Spiegel, S. Stoynev, J. Strait, N. Strobbe, L. Taylor, S. Tkaczyk, N.V. Tran, L. Uplegger, E.W. Vaandering, C. Vernieri, M. Verzocchi, R. Vidal, M. Wang, H.A. Weber, A. Whitbeck, W. Wu

University of Florida, Gainesville, USA

D. Acosta, P. Avery, P. Bortignon, D. Bourilkov, A. Brinkerhoff, A. Carnes, M. Carver, D. Curry, R.D. Field, I.K. Furic, S.V. Gleyzer, B.M. Joshi, J. Konigsberg, A. Korytov, K. Kotov, P. Ma, K. Matchev, H. Mei, G. Mitselmakher, K. Shi, D. Sperka, N. Terentyev, L. Thomas, J. Wang, S. Wang, J. Yelton

Florida International University, Miami, USA

Y.R. Joshi, S. Linn, P. Markowitz, J.L. Rodriguez

Florida State University, Tallahassee, USA

A. Ackert, T. Adams, A. Askew, S. Hagopian, V. Hagopian, K.F. Johnson, T. Kolberg, G. Martinez, T. Perry, H. Prosper, A. Saha, A. Santra, V. Sharma, R. Yohay

Florida Institute of Technology, Melbourne, USA

M.M. Baarmand, V. Bhopatkar, S. Colafranceschi, M. Hohlmann, D. Noonan, T. Roy, F. Yumiceva

University of Illinois at Chicago (UIC), Chicago, USA

M.R. Adams, L. Apanasevich, D. Berry, R.R. Betts, R. Cavanaugh, X. Chen, S. Dittmer, O. Ev-

dokimov, C.E. Gerber, D.A. Hangal, D.J. Hofman, K. Jung, J. Kamin, I.D. Sandoval Gonzalez, M.B. Tonjes, N. Varelas, H. Wang, Z. Wu, J. Zhang

The University of Iowa, Iowa City, USA

B. Bilki⁶⁷, W. Clarida, K. Dilsiz⁶⁸, S. Durgut, R.P. Gandrajula, M. Haytmyradov, V. Khristenko, J.-P. Merlo, H. Mermerkaya⁶⁹, A. Mestvirishvili, A. Moeller, J. Nachtman, H. Ogul⁷⁰, Y. Onel, F. Ozok⁷¹, A. Penzo, C. Snyder, E. Tiras, J. Wetzel, K. Yi

Johns Hopkins University, Baltimore, USA

B. Blumenfeld, A. Cocoros, N. Eminizer, D. Fehling, L. Feng, A.V. Gritsan, W.T. Hung, P. Maksimovic, J. Roskes, U. Sarica, M. Swartz, M. Xiao, C. You

The University of Kansas, Lawrence, USA

A. Al-bataineh, P. Baringer, A. Bean, S. Boren, J. Bowen, J. Castle, S. Khalil, A. Kropivnitskaya, D. Majumder, W. Mcbrayer, M. Murray, C. Rogan, C. Royon, S. Sanders, E. Schmitz, J.D. Tapia Takaki, Q. Wang

Kansas State University, Manhattan, USA

A. Ivanov, K. Kaadze, Y. Maravin, A. Modak, A. Mohammadi, L.K. Saini, N. Skhirtladze

Lawrence Livermore National Laboratory, Livermore, USA

F. Rebassoo, D. Wright

University of Maryland, College Park, USA

A. Baden, O. Baron, A. Belloni, S.C. Eno, Y. Feng, C. Ferraioli, N.J. Hadley, S. Jabeen, G.Y. Jeng, R.G. Kellogg, J. Kunkle, A.C. Mignerey, F. Ricci-Tam, Y.H. Shin, A. Skuja, S.C. Tonwar

Massachusetts Institute of Technology, Cambridge, USA

D. Abercrombie, B. Allen, V. Azzolini, R. Barbieri, A. Baty, G. Bauer, R. Bi, S. Brandt, W. Busza, I.A. Cali, M. D'Alfonso, Z. Demiragli, G. Gomez Ceballos, M. Goncharov, P. Harris, D. Hsu, M. Hu, Y. Iiyama, G.M. Innocenti, M. Klute, D. Kovalskyi, Y.-J. Lee, A. Levin, P.D. Luckey, B. Maier, A.C. Marini, C. Mcginn, C. Mironov, S. Narayanan, X. Niu, C. Paus, C. Roland, G. Roland, G.S.F. Stephans, K. Sumorok, K. Tatar, D. Velicanu, J. Wang, T.W. Wang, B. Wyslouch, S. Zhaozhong

University of Minnesota, Minneapolis, USA

A.C. Benvenuti, R.M. Chatterjee, A. Evans, P. Hansen, S. Kalafut, Y. Kubota, Z. Lesko, J. Mans, S. Nourbakhsh, N. Ruckstuhl, R. Rusack, J. Turkewitz, M.A. Wadud

University of Mississippi, Oxford, USA

J.G. Acosta, S. Oliveros

University of Nebraska-Lincoln, Lincoln, USA

E. Avdeeva, K. Bloom, D.R. Claes, C. Fangmeier, F. Golf, R. Gonzalez Suarez, R. Kamalieddin, I. Kravchenko, J. Monroy, J.E. Siado, G.R. Snow, B. Stieger

State University of New York at Buffalo, Buffalo, USA

A. Godshalk, C. Harrington, I. Iashvili, D. Nguyen, A. Parker, S. Rappoccio, B. Roozbahani

Northeastern University, Boston, USA

G. Alverson, E. Barberis, C. Freer, A. Hortiangtham, A. Massironi, D.M. Morse, T. Orimoto, R. Teixeira De Lima, T. Wamorkar, B. Wang, A. Wisecarver, D. Wood

Northwestern University, Evanston, USA

S. Bhattacharya, O. Charaf, K.A. Hahn, N. Mucia, N. Odell, M.H. Schmitt, K. Sung, M. Trovato, M. Velasco

University of Notre Dame, Notre Dame, USA

R. Bucci, N. Dev, M. Hildreth, K. Hurtado Anampa, C. Jessop, D.J. Karmgard, N. Kellams, K. Lannon, W. Li, N. Loukas, N. Marinelli, F. Meng, C. Mueller, Y. Musienko³⁶, M. Planer, A. Reinsvold, R. Ruchti, P. Siddireddy, G. Smith, S. Taroni, M. Wayne, A. Wightman, M. Wolf, A. Woodard

The Ohio State University, Columbus, USA

J. Alimena, L. Antonelli, B. Bylsma, L.S. Durkin, S. Flowers, B. Francis, A. Hart, C. Hill, W. Ji, T.Y. Ling, W. Luo, B.L. Winer, H.W. Wulsin

Princeton University, Princeton, USA

S. Cooperstein, O. Driga, P. Elmer, J. Hardenbrook, P. Hebda, S. Higginbotham, A. Kalogeropoulos, D. Lange, J. Luo, D. Marlow, K. Mei, I. Ojalvo, J. Olsen, C. Palmer, P. Piroué, J. Salfeld-Nebgen, D. Stickland, C. Tully

University of Puerto Rico, Mayaguez, USA

S. Malik, S. Norberg

Purdue University, West Lafayette, USA

A. Barker, V.E. Barnes, S. Das, L. Gutay, M. Jones, A.W. Jung, A. Khatiwada, D.H. Miller, N. Neumeister, C.C. Peng, H. Qiu, J.F. Schulte, J. Sun, F. Wang, R. Xiao, W. Xie

Purdue University Northwest, Hammond, USA

T. Cheng, J. Dolen, N. Parashar

Rice University, Houston, USA

Z. Chen, K.M. Ecklund, S. Freed, F.J.M. Geurts, M. Guilbaud, M. Kilpatrick, W. Li, B. Michlin, B.P. Padley, J. Roberts, J. Rorie, W. Shi, Z. Tu, J. Zabel, A. Zhang

University of Rochester, Rochester, USA

A. Bodek, P. de Barbaro, R. Demina, Y.t. Duh, T. Ferbel, M. Galanti, A. Garcia-Bellido, J. Han, O. Hindrichs, A. Khukhunaishvili, K.H. Lo, P. Tan, M. Verzetti

The Rockefeller University, New York, USA

R. Ciesielski, K. Goulianos, C. Mesropian

Rutgers, The State University of New Jersey, Piscataway, USA

A. Agapitos, J.P. Chou, Y. Gershtein, T.A. Gómez Espinosa, E. Halkiadakis, M. Heindl, E. Hughes, S. Kaplan, R. Kunnawalkam Elayavalli, S. Kyriacou, A. Lath, R. Montalvo, K. Nash, M. Osherson, H. Saka, S. Salur, S. Schnetzer, D. Sheffield, S. Somalwar, R. Stone, S. Thomas, P. Thomassen, M. Walker

University of Tennessee, Knoxville, USA

A.G. Delannoy, J. Heideman, G. Riley, K. Rose, S. Spanier, K. Thapa

Texas A&M University, College Station, USA

O. Bouhali⁷², A. Castaneda Hernandez⁷², A. Celik, M. Dalchenko, M. De Mattia, A. Delgado, S. Dildick, R. Eusebi, J. Gilmore, T. Huang, T. Kamon⁷³, R. Mueller, Y. Pakhotin, R. Patel, A. Perloff, L. Perniè, D. Rathjens, A. Safonov, A. Tatarinov

Texas Tech University, Lubbock, USA

N. Akchurin, J. Damgov, F. De Guio, P.R. Duderov, J. Faulkner, E. Gurpinar, S. Kunori, K. Lamichhane, S.W. Lee, T. Mengke, S. Muthumuni, T. Peltola, S. Undleeb, I. Volobouev, Z. Wang

Vanderbilt University, Nashville, USA

S. Greene, A. Gurrola, R. Janjam, W. Johns, C. Maguire, A. Melo, H. Ni, K. Padeken, J.D. Ruiz Alvarez, P. Sheldon, S. Tuo, J. Velkovska, Q. Xu

University of Virginia, Charlottesville, USA

M.W. Arenton, P. Barria, B. Cox, R. Hirosky, M. Joyce, A. Ledovskoy, H. Li, C. Neu, T. Sinthuprasith, Y. Wang, E. Wolfe, F. Xia

Wayne State University, Detroit, USA

R. Harr, P.E. Karchin, N. Poudyal, J. Sturdy, P. Thapa, S. Zaleski

University of Wisconsin - Madison, Madison, WI, USA

M. Brodski, J. Buchanan, C. Caillol, D. Carlsmith, S. Dasu, L. Dodd, S. Duric, B. Gomber, M. Grothe, M. Herndon, A. Hervé, U. Hussain, P. Klabbers, A. Lanaro, A. Levine, K. Long, R. Loveless, V. Rekovic, T. Ruggles, A. Savin, N. Smith, W.H. Smith, N. Woods

†: Deceased

1: Also at Vienna University of Technology, Vienna, Austria

2: Also at IRFU; CEA; Université Paris-Saclay, Gif-sur-Yvette, France

3: Also at Universidade Estadual de Campinas, Campinas, Brazil

4: Also at Federal University of Rio Grande do Sul, Porto Alegre, Brazil

5: Also at Universidade Federal de Pelotas, Pelotas, Brazil

6: Also at Université Libre de Bruxelles, Bruxelles, Belgium

7: Also at Institute for Theoretical and Experimental Physics, Moscow, Russia

8: Also at Joint Institute for Nuclear Research, Dubna, Russia

9: Also at Helwan University, Cairo, Egypt

10: Now at Zewail City of Science and Technology, Zewail, Egypt

11: Now at Cairo University, Cairo, Egypt

12: Also at Department of Physics; King Abdulaziz University, Jeddah, Saudi Arabia

13: Also at Université de Haute Alsace, Mulhouse, France

14: Also at Skobeltsyn Institute of Nuclear Physics; Lomonosov Moscow State University, Moscow, Russia

15: Also at CERN; European Organization for Nuclear Research, Geneva, Switzerland

16: Also at RWTH Aachen University; III. Physikalisches Institut A, Aachen, Germany

17: Also at University of Hamburg, Hamburg, Germany

18: Also at Brandenburg University of Technology, Cottbus, Germany

19: Also at Institute of Nuclear Research ATOMKI, Debrecen, Hungary

20: Also at MTA-ELTE Lendület CMS Particle and Nuclear Physics Group; Eötvös Loránd University, Budapest, Hungary

21: Also at Institute of Physics; University of Debrecen, Debrecen, Hungary

22: Also at Indian Institute of Technology Bhubaneswar, Bhubaneswar, India

23: Also at Institute of Physics, Bhubaneswar, India

24: Also at Shoolini University, Solan, India

25: Also at University of Visva-Bharati, Santiniketan, India

26: Also at University of Ruhuna, Matara, Sri Lanka

27: Also at Isfahan University of Technology, Isfahan, Iran

28: Also at Yazd University, Yazd, Iran

29: Also at Plasma Physics Research Center; Science and Research Branch; Islamic Azad University, Tehran, Iran

30: Also at Università degli Studi di Siena, Siena, Italy

31: Also at INFN Sezione di Milano-Bicocca; Università di Milano-Bicocca, Milano, Italy

- 32: Also at International Islamic University of Malaysia, Kuala Lumpur, Malaysia
- 33: Also at Malaysian Nuclear Agency; MOSTI, Kajang, Malaysia
- 34: Also at Consejo Nacional de Ciencia y Tecnología, Mexico city, Mexico
- 35: Also at Warsaw University of Technology; Institute of Electronic Systems, Warsaw, Poland
- 36: Also at Institute for Nuclear Research, Moscow, Russia
- 37: Now at National Research Nuclear University 'Moscow Engineering Physics Institute' (MEPhI), Moscow, Russia
- 38: Also at St. Petersburg State Polytechnical University, St. Petersburg, Russia
- 39: Also at University of Florida, Gainesville, USA
- 40: Also at P.N. Lebedev Physical Institute, Moscow, Russia
- 41: Also at California Institute of Technology, Pasadena, USA
- 42: Also at Budker Institute of Nuclear Physics, Novosibirsk, Russia
- 43: Also at Faculty of Physics; University of Belgrade, Belgrade, Serbia
- 44: Also at INFN Sezione di Pavia; Università di Pavia, Pavia, Italy
- 45: Also at University of Belgrade; Faculty of Physics and Vinca Institute of Nuclear Sciences, Belgrade, Serbia
- 46: Also at Scuola Normale e Sezione dell'INFN, Pisa, Italy
- 47: Also at National and Kapodistrian University of Athens, Athens, Greece
- 48: Also at Riga Technical University, Riga, Latvia
- 49: Also at Universität Zürich, Zurich, Switzerland
- 50: Also at Stefan Meyer Institute for Subatomic Physics (SMI), Vienna, Austria
- 51: Also at Adiyaman University, Adiyaman, Turkey
- 52: Also at Istanbul Aydin University, Istanbul, Turkey
- 53: Also at Mersin University, Mersin, Turkey
- 54: Also at Piri Reis University, Istanbul, Turkey
- 55: Also at Izmir Institute of Technology, Izmir, Turkey
- 56: Also at Necmettin Erbakan University, Konya, Turkey
- 57: Also at Marmara University, Istanbul, Turkey
- 58: Also at Kafkas University, Kars, Turkey
- 59: Also at Istanbul Bilgi University, Istanbul, Turkey
- 60: Also at Rutherford Appleton Laboratory, Didcot, United Kingdom
- 61: Also at School of Physics and Astronomy; University of Southampton, Southampton, United Kingdom
- 62: Also at Monash University; Faculty of Science, Clayton, Australia
- 63: Also at Instituto de Astrofísica de Canarias, La Laguna, Spain
- 64: Also at Bethel University, ST. PAUL, USA
- 65: Also at Utah Valley University, Orem, USA
- 66: Also at Purdue University, West Lafayette, USA
- 67: Also at Beykent University, Istanbul, Turkey
- 68: Also at Bingol University, Bingol, Turkey
- 69: Also at Erzincan University, Erzincan, Turkey
- 70: Also at Sinop University, Sinop, Turkey
- 71: Also at Mimar Sinan University; Istanbul, Istanbul, Turkey
- 72: Also at Texas A&M University at Qatar, Doha, Qatar
- 73: Also at Kyungpook National University, Daegu, Korea